



Micro-scale geochemical and crystallographic analysis of *Buccinum undatum* statoliths supports an annual periodicity of growth ring deposition

Hollyman, Philip; Chenery, Simon; Ignatyev, Constantin; Laptikhovsky, Vladimir; Richardson, Christopher

Chemical Geology

DOI:
[10.1016/j.chemgeo.2017.09.034](https://doi.org/10.1016/j.chemgeo.2017.09.034)

Published: 05/11/2019

Peer reviewed version

[Cyswllt i'r cyhoeddiad / Link to publication](#)

Dyfyniad o'r fersiwn a gyhoeddwyd / Citation for published version (APA):
Hollyman, P., Chenery, S., Ignatyev, C., Laptikhovsky, V., & Richardson, C. (2019). Micro-scale geochemical and crystallographic analysis of *Buccinum undatum* statoliths supports an annual periodicity of growth ring deposition. *Chemical Geology*, 526, 153-164.
<https://doi.org/10.1016/j.chemgeo.2017.09.034>

Hawliau Cyffredinol / General rights

Copyright and moral rights for the publications made accessible in the public portal are retained by the authors and/or other copyright owners and it is a condition of accessing publications that users recognise and abide by the legal requirements associated with these rights.

- Users may download and print one copy of any publication from the public portal for the purpose of private study or research.
- You may not further distribute the material or use it for any profit-making activity or commercial gain
- You may freely distribute the URL identifying the publication in the public portal ?

Take down policy

If you believe that this document breaches copyright please contact us providing details, and we will remove access to the work immediately and investigate your claim.

1 Highlights

- 2 • *Buccinum undatum* statoliths were found to be wholly aragonitic at 2µm resolution
- 3 • Differing XRD patterns indicate changes in structural complexity across statoliths, confirmed
- 4 via SEM to be due to an 'hourglass' microstructure
- 5 • Clear cycles of Mg and Na found between statolith growth rings using SIMS, supporting an
- 6 annual periodicity
- 7 • Mg and Na profiles were found to be anti-correlated in all specimens
- 8 • Each individual displayed substantial ontogenetic change in strontium concentration

9

10

11

12

13

14

15

16

17

18

19

20

21

22

23

24

25

26

27

28

29

30 **Micro-scale geochemical and crystallographic analysis of *Buccinum undatum* statoliths**
31 **supports an annual periodicity of growth ring deposition.**

32 Philip R. Hollyman^{1*}, Simon R. N. Chenery², EIMF³, Konstantin Ignatyev⁴, Vladimir V.
33 Laptikhovskiy⁵, Christopher A. Richardson¹.

34 1) School of Ocean Sciences, College of Natural Sciences, Bangor University, Menai Bridge,
35 Anglesey, LL59 5AB, UK

36 2) Centre for Environmental Geochemistry, British Geological Survey (BGS), Nottingham,
37 NG12 5GG, UK

38 3) Edinburgh Ion Microprobe Facility (EIMF), School of Geosciences, Grant Institute,
39 Edinburgh University, Edinburgh, EH9 3FE, UK

40 4) Diamond Light Source, Diamond House, Harwell Science and Innovation Campus, Fermi
41 Ave, Didcot, OX11 0DE, UK

42 5) Centre for Environment, Fisheries and Aquaculture Science (CEFAS), Pakefield Road,
43 Lowestoft, Suffolk NR33 0HT, UK

44

45 *Corresponding Author: p.hollyman@bangor.ac.uk

46 **Abstract**

47 The whelk *Buccinum undatum* is commercially important in the North Atlantic. However,
48 monitoring the ontogenetic age and growth of populations has been problematic for fisheries
49 scientists owing to the lack of a robust age determination method. We confirmed the annual
50 periodicity of growth rings present in calcified statoliths located in the foot of field-collected
51 and laboratory reared whelks using microscale measurements of trace element
52 geochemistry. Using Secondary Ion Mass Spectrometry (SIMS), annual trace element profiles
53 were quantified at 2 μm resolution in statoliths removed from whelks collected alive from
54 three locations spanning the length of the UK; the Shetland Isles (North), the Menai Strait,
55 North Wales (Mid) and Jersey (South). Clear cycles in the Mg/Ca ratio were apparent with
56 minimum values corresponding with the visible dark statolith rings and comparatively higher
57 ratios displayed in the first year of growth. Statoliths from one and two-year-old laboratory
58 reared whelks of known age and life history contained one and two Mg/Ca cycles respectively
59 and demonstrated that the statolith growth ring is formed during winter (February and

60 March). Cycles of Na/Ca were found to be anti-correlated to Mg/Ca cycles, whilst ratios of
61 Sr/Ca were inconsistent and showed an apparent ontogenetic increase, suggesting strong
62 physiological control. Variability in elemental data will likely limit the usefulness of these
63 structures as environmental recorders. The results obtained using SIMS for trace element
64 analysis of statoliths confirms the robustness of the statolith rings in estimating whelk age.
65 μ XRD at 2 μ m spatial resolution demonstrated the statoliths were wholly aragonitic and thus
66 trace element variation was not the result of possible differences in CaCO₃ polymorph within
67 the statolith. Changing XRD patterns along with SEM imaging also reveal an 'hourglass'
68 microstructure within each statolith. The validation of the annual periodicity of statolith
69 growth rings now provides a robust and novel age determination technique that will lead to
70 improved management of *B. undatum* stocks.

71 Keywords: Statolith, Age determination, SIMS, μ XRD, Magnesium, Strontium, Sodium

72 **1. Introduction**

73 Statoliths have previously been investigated in several invertebrate groups including squid
74 (Arkhipkin, 2005), octopods (Lombarte *et al.*, 2006), cuttlefish (Gillanders *et al.*, 2013),
75 jellyfish (Mooney & Kingsford, 2017) and gastropods (Richardson *et al.*, 2005; Chatzinikolaou
76 & Richardson 2007; Hollyman *et al.*, 2017). These small calcium carbonate bodies are involved
77 in the perception of gravity (Chase, 2002) within the nervous system of many mobile mollusc
78 species (e.g. cephalopods and gastropods). The statoliths of gastropods can contain several
79 types of growth increments that have been shown to represent annual rings, settlement rings
80 in species with planktonic larvae (e.g. *Nassarius reticulatus* [Barroso *et al.*, 2005; Chatzinikolaou
81 & Richardson, 2007], *Polinices pulchellus* [Richardson *et al.*, 2005]); and hatching rings in
82 direct developing species (e.g. *Buccinum undatum* [Hollyman *et al.*, 2017]). These growth

83 rings are perturbations in the microstructure visible during observation using an optical
84 microscope. They are thought to be a result of changing growth rates, resulting in 'light' and
85 'dark' areas of the structure, much like growth banding patterns in bivalve shells (see
86 Richardson, 2001 for review). The potential of these structures as tools to determine
87 ontogenetic age is great within the context of fisheries management. *B. undatum* is a
88 commercially important species of neogastropod mollusc common to the waters of the North
89 Atlantic. The global fishery for *B. undatum* has increased dramatically over the last 30 years
90 with landings in the UK (as an example) rising from just over 8,000 t in 2003 (DEFRA, 2003) to
91 over 20,000 t in 2015 (MMO, 2016). *B. undatum* poses a problem to fisheries scientists as they
92 display a variable size-at-maturity, and potentially size-at-age over relatively small
93 geographical distances (Shelmerdine *et al.*, 2007; Haig *et al.*, 2015; McIntyre *et al.*, 2015). The
94 lack of a reliable age determination tool makes it difficult for fisheries scientists to monitor
95 and assess *B. undatum* populations.

96 Recent work on the statoliths of the whelk, *B. undatum*, has highlighted a potential annual
97 periodicity to prominent growth rings through a series of laboratory growth experiments and
98 chemical analysis of the shells (Hollyman *et al.*, 2017); no direct chemical analysis of statoliths
99 from this species has been undertaken. Galante-Oliveira *et al.* (2015) highlighted for the first
100 time an annual periodicity to growth rings in the statoliths of the netted whelk, *N. reticulatus*,
101 using Laser Ablation – Inductively Coupled Plasma – Mass Spectrometry (LA-ICP-MS) to
102 identify annual cycles of strontium (Sr). Analysis of trace elements such as Sr and magnesium
103 (Mg) in the statoliths of *B. undatum* could provide a robust method for establishing the
104 number of seasonal cycles and the validation of the annual periodicity of growth ring
105 deposition, as well as assessing their potential as environmental recorders.

106 During formation, mollusc carbonates can 'record' certain environmental conditions in the
107 concentrations of incorporated trace elements (i.e. elements other than Ca, C and O). Certain
108 trace elements can become incorporated into the calcium carbonate crystals through the
109 substitution of Ca^{2+} for other divalent metal ions with similar atomic radii (Speer *et al.*, 1983;
110 Dietzel *et al.*, 2004). The rhombohedral crystal lattice of calcite may incorporate the slightly
111 smaller magnesium (Mg^{2+}) ion at higher concentrations than the orthorhombic structure of
112 aragonite, which can incorporate the slightly larger strontium ion (Sr^{2+}) at higher
113 concentrations than calcite (Speer *et al.*, 1983; Dietzel *et al.*, 2004; Schöne *et al.*, 2010). For
114 ions such as Na^+ which has a similar size to Ca^{2+} but a different charge, it is thought that a
115 charge balance is created by either incorporating trivalent ions such as Al^{3+} or Fe^{3+} (Billings &
116 Ragland, 1968), or a carbonate ion (CO_3^{2-}) with a monovalent halide ion (e.g. F^- , Cl^- , Br^- or I^-
117 [Yoshimura *et al.*, 2017]). Molluscs have been shown to produce several polymorphs of CaCO_3
118 within a single bivalve mollusc shell (Nehrke *et al.*, 2012) and gastropod statolith (Galante-
119 Oliveira *et al.*, 2014). It is therefore imperative to understand the mineralogical composition
120 of a skeletal hard part before attempting to interpret the results of trace element analyses.

121 Strontium and Magnesium concentrations in both calcite and aragonite have the potential to
122 reflect ambient seawater temperature at the time of mineralisation. It has been shown that
123 in abiogenic aragonite Sr/Ca and Mg/Ca ratios have a negative relationship with seawater
124 temperature, i.e. with increasing temperature the concentration of Sr and Mg decreases
125 (Kinsman & Holland, 1969; Gaetani & Cohen, 2006); the opposite of this is seen with Mg in
126 abiogenic calcite (Katz, 1973; Mucci, 1987). In mollusc carbonates, this relationship between
127 Sr and seawater temperature has been shown to be negative in species with aragonitic
128 structures (e.g. *Mytilus sp.* [Dodd, 1965]; *Arctica islandica* [Schöne *et al.*, 2011]; *Tridacna gigas*

129 [Yan *et al.*, 2013]). An opposite relationship was demonstrated in the aragonitic shells of the
130 marine gastropod *Conus ermenius*, where Sr has been shown to be positively correlated with
131 seawater temperature (Sosdian *et al.*, 2006; Gentry *et al.*, 2008). Magnesium has also been
132 shown to vary with seawater temperature in the shells of several marine bivalves (e.g. *Mytilus*
133 *sp.* [Dodd, 1965]; *Pinna noblis*, during early ontogeny [Freitas *et al.*, 2005]; *Crassostrea*
134 *virginica* and *Magallana gigas* [Durham *et al.*, 2017]). The efficacy of quantifying the
135 concentration of trace elements such as Sr and Mg, and using these as proxies for seawater
136 temperature is controversial, with large discrepancies seen between species and within
137 individual samples (Klein *et al.*, 1996; Purton *et al.*, 1999). There are many factors which can
138 potentially affect trace element incorporation, influences which stem from physiological
139 sources such as ontogeny, growth rate, and stress are often termed vital effects. Vital effects
140 can control trace element incorporation and result in dis-equilibrium of trace elements
141 (within the carbonate) from ambient elemental concentrations in the seawater at the time of
142 formation (Richardson, 2001; Gillikin *et al.*, 2005; Sosidan *et al.*, 2006). This can ‘override’ the
143 temperature control on trace element incorporation, removing (or altering) any temperature
144 signal which may have been contained within the trace element record. Whilst trace element
145 profiles within mollusc shells are sometimes unsuitable for accurate seawater temperature
146 reconstructions due to factors such as vital effects, seasonal cycles in element profiles may
147 still be evident, allowing an age to be assigned to an individual animal (e.g. Durham *et al.*,
148 2017).

149 Here we assess the potential of *B. undatum* statoliths as both life history and environmental
150 proxy archives. This is approached by firstly determining the overall structure of the statoliths
151 and presence and position of any CaCO₃ polymorph changes. It was hypothesized that the

152 statoliths would be comprised of a majority aragonite fraction. The trace element profiles of
153 statoliths from several discrete locations were then analysed and compared to investigate
154 their potential as environmental and life history recorders. It was hypothesized that clearly
155 delineated cycles of Sr and Mg would be uncovered between the visible 'annual' growth rings,
156 following the work of Galante-Oliveira *et al.* (2015).

157 **2. Materials and Methods**

158 Three sampling sites were chosen within the United Kingdom (U.K.). The Shetland Isles
159 (Northern Scotland), the Menai Strait (North Wales) and southern Jersey (English Channel)
160 represent cool, mid-range and warm sites respectively owing to their differing seawater
161 temperature regimes (Figure 1). *Buccinum undatum* were collected during winter (February)
162 2015, using baited whelk pots deployed from local fishing boats and left to soak for 24 hours.
163 The depth at each site ranged between 11 and 18 m (Shetland – 18 m, Menai Strait – 11 m,
164 Jersey – 13 m).

165 Whelks from the three sites (Figure 1) were selected for trace element analysis based on the
166 largest size in the population (to give the longest growth axis for elemental analysis) and best
167 shell condition (e.g. undamaged, i.e. unbored by organisms and not chipped and repaired).
168 Shell damage and repair in the form of scars on the shell surface is likely translated into more
169 disturbance rings in the statolith (Hollyman *et al.*, 2017), conversely less damage likely results
170 in fewer disturbance rings in the statolith on a site by site basis. Based on their gonad maturity
171 stage (see Haig *et al.*, 2015) three mature male and three mature female whelks were chosen
172 from each site. Furthermore, shells of juvenile laboratory-reared whelks sampled in 2015 that
173 hatched from egg masses in 2013 (two-year old) and 2014 (one-year old) (see Hollyman *et al.*,
174 2017) were selected for analysis. Six whelks from the 2013 cohort representing both smaller

175 than average sized individuals (three of ~35 mm shell length) and larger than average
176 individuals (three of ~50 mm shell length) and a similar group of whelks from the 2014 cohort
177 (three smaller than average ~10 mm shell length; three larger than average ~30 mm shell
178 length) were selected for analysis.

179 Prior to statolith extraction all dissection tools and glassware were acid-cleaned to avoid
180 contamination. Both left and right statoliths were extracted (see Hollyman *et al.* 2017), placed
181 into an embryo dish, rinsed with ultra-pure 18.2M Ω water (www.millipore.com; hereafter
182 referred to as Milli-Q water) and immersed in 30% (by volume) hydrogen peroxide for 30
183 minutes. Following cleaning, statoliths were thoroughly rinsed again in Milli-Q water and left
184 to dry overnight in a laminar flow hood. Thirty pairs of statoliths from the field and laboratory
185 samples were analysed to investigate the crystal- and microstructure of the statoliths as well
186 as how the trace element profiles changed along the growth axis in relation to visible annual
187 growth rings.

188 2.1. *Transmission micro X-Ray Diffraction (μ XRD)*

189 The right statolith from each specimen were embedded in Buehler EpoThin 2™ resin on
190 standard microscope slides and left to cure for 72 hours. Once set, the statoliths were ground
191 by hand towards their centre to expose the nucleus using successive grades of silicon carbide
192 grinding paper (FEPA P400, P1200 & P2500 grade). Once a plane ~15 μ m from the central
193 nucleus was reached, the resin block was carefully removed from the microscope slide with a
194 scalpel and turned over, the ground surface was then glued onto the slide and the grinding
195 process was repeated to produce a thin section (~25-30 μ m thickness) of each statolith. These
196 thin statolith sections were subsequently removed from the slide using acetone to dissolve
197 the glue and cleaned in 70% (ABV) ethanol and Milli-Q water. Each thin section was then

198 mounted on Kapton (poly (4,4'-oxydiphenylene-pyromellitimide)) tape and suspended over
199 'windows' in custom microscope slides to allow for interference free transmission analysis.
200 Each sample was imaged using a Meiji Techno MT8100 microscope with a Lumenera Infinity
201 3 microscope camera at x2.5 and x20 magnifications.

202 Using the I-18 micro-spectroscopy beamline at the Diamond Light Source (DLS), a 2x2 μ m X-
203 ray beam was used with a sample transition step size of 2 μ m to create a line profile across
204 the centre of each statolith to investigate any polymorph changes in the calcium carbonate
205 phase. An X-ray beam energy of 12 KeV was employed and a Photonics Science SCMOS
206 camera was used to collect the diffraction images. Diffraction data were collected as 2D
207 diffraction images and converted to intensity vs. d-spacing plots using the angle of incidence
208 (θ , θ) and the wavelength of the X-ray beam (λ , λ) and the following equation:

209 $n * \lambda = 2d * \sin(\theta)$, (Bragg, 1913).

210 d-spacing values represent the distance between the atomic layers in a crystal. Crystalline
211 substances produce unique d-spacing intensity spectra and so this method can be used to
212 distinguish between polymorphs of crystalline calcium carbonate. Standards of silicon and
213 lanthanum hexaboride (LaB₆) powders were used to calibrate the detector geometry to
214 determine θ . Powdered synthetic calcite and speleothem aragonite were also analysed for
215 direct comparison to the statolith samples (Brinza *et al.*, 2014). A continuous analysis was
216 taken for 15 seconds whilst rastering across the powdered calcium carbonate standards to
217 maximise the number of crystal orientations available for comparison to the subsequent
218 statolith samples. To confirm that no compositional changes had been caused within the
219 statoliths during physical sample preparation, several XRD samples were taken of unmounted
220 broken statoliths. This control analysis was undertaken to ensure that potential heat

221 generated during grinding did not cause a polymorph change from aragonite to calcite (Radha
222 *et al.*, 2010; Gong *et al.*, 2012; Galante-Oliveira *et al.*, 2014). To investigate potential damage
223 to the statolith during μ XRD analysis, prolonged exposure to the X-ray beam was conducted
224 at two points on the same statolith thin section, in the centre and at the outer edge. The beam
225 was held on a single spot for 120 seconds, taking a separate diffraction pattern every 10
226 seconds to look for changes in structure over time. The scatter background was minimised
227 using a rolling ball baseline correction; all data processing was completed in Dawn 1.9.0
228 (Basham *et al.*, 2015). Due to time constraints, only statoliths from 18 of the total 30
229 specimens were analysed using μ XRD. These 18 samples were comprised of representative
230 specimens of all sites, sexes and both laboratory reared cohorts.

231 2.2. Scanning Electron Microscopy (SEM)

232 Statolith fragments were imaged using SEM to investigate microstructure as follows.
233 Statoliths were placed in a watch glass and broken into fragments using fine tipped forceps
234 (0.10 x 0.06mm tip) and selected pieces (the largest segments with full, exposed internal
235 planes) mounted on Kapton tape. The statolith fragments were imaged using an FEI QUANTA
236 600 environmental scanning electron microscope (SEM) operated in low vacuum mode, with
237 an electron beam accelerating voltage of 12.5 - 15 kV, a beam probe current of \sim 20 nA, and a
238 working distance of \sim 10 mm.

239 2.3. Secondary Ion Mass Spectrometry (SIMS)

240 The left statolith from each animal was embedded in Buehler EpoThin 2™ resin in 1-inch round
241 blocks, directly onto a 1-inch round microscope slide with a single statolith per block and left
242 to cure for 72 hours. The resin blocks were then ground by hand through P400, P1200, P2500

243 and P4000 (FEPA) grade silicon carbide grinding papers using Milli-Q water as lubricant. This
244 produced a thin section exposing the central plane of each statolith (Figure 2). Following
245 grinding, two grades of diamond gel polish (3 μ m & 1 μ m, Presi) were used in conjunction with
246 a Memphis polishing cloth (Metprep). Each slide was then imaged using a Meiji Techno
247 MT8100 microscope with a Lumenera Infinity 3 microscope camera at varying magnifications
248 (x10, x20 and x40) to create maps for the SIMS analysis. Each slide was then gold coated prior
249 to analysis to minimise charging effects.

250 SIMS analysis was carried out using a CAMECA IMS-4f Ion Microprobe with a primary negative
251 ion beam ($^{16}\text{O}^-$) from a duoplasmatron source at the Edinburgh Ion Microprobe Facility (EIMF).
252 Samples were pumped to a vacuum of 5×10^{-9} Torr and a pre-ablation path was cleaned via a
253 beam current of 6 nA with a net input energy of 15KeV using a primary aperture to give a
254 beam size of $\sim 25 \mu\text{m}$. The sample was moved beneath the beam in 10 μm steps to remove
255 gold and pre-condition the statolith surface. Following this, a continuous sample track was
256 made across the pre-conditioned section of each statolith using a primary aperture and a
257 beam current of 0.06 nA with a net input energy of 15KeV; this gave a spot size of $\sim 1\text{-}2 \mu\text{m}$, a
258 25 μm image field was used and no energy filtering was employed. The sample was moved
259 beneath the beam in 2 μm steps to create a successive spot sample track. Five elements were
260 quantified across the growth axis of each statolith: ^{27}Al (to monitor contamination), ^{44}Ca (to
261 which all trace elements were compared to create a ratio), ^{23}Na , ^{88}Sr and ^{24}Mg . Ca was
262 assumed to be stoichiometric and constant, all other elements are presented as their ratio to
263 ^{44}Ca . Initially ^7Li and ^{138}Ba were analysed in a single statolith, but the concentrations were
264 found to be low and showed no variation above the counting statistic errors, suggesting
265 quantitative data would not be obtainable under these analytical conditions. Thus, these

266 elements were not analysed in other statoliths. Elemental ratios were calculated using
267 working curves based on standards previously analysed by bulk techniques, which included a
268 mixture of abiogenic and biogenic carbonates (Corals: M93 [Kasemann *et al.*, 2009], Haxby
269 [Sturrock *et al.*, 2015]; OKA carbonatite [Bice *et al.*, 2005]; Icelandic spar) and a magnesium
270 rich dolomite standard. Although no corrections were made, at the concentrations measured
271 the molecular or doubly charged ion species e.g. $^{48}\text{Ca}^{2+}$ overlap on ^{24}Mg were considered
272 negligible from measured standard samples. Estimated interference of Ca^{2+} at mass 24 was <
273 0.002 mmol/mol and Ca_2^+ at mass 88 = 0.02 mmol/mol. Accuracy was better than 10% and
274 the precision errors for the analysed elements are as follows: Na ~1% (two sigma), Mg ~4.5%
275 (two sigma), Ca ~1.1% (two sigma) and Sr ~1.4% (two sigma).

276 Elemental data were compared between and within sites using ANOVA in R (R core team,
277 2017). For Mg/Ca data, peak heights were compiled from all samples at a single site and
278 compared between sites to check for between site differences in Mg/Ca peaks, any
279 anomalous peaks were discounted from the analysis. For Sr/Ca ratios, the outer 10 data points
280 from each statolith from each site were compiled and compared to the compiled central 10
281 data points from the same specimens to check for ontogenetic changes, these data were not
282 compared between sites. The normal distribution of the data from each dataset was
283 confirmed using Shapiro-Wilk tests.

284 **3. Results**

285 **3.1. *Statolith crystallography and microstructure***

286 μXRD was used to investigate micro-scale changes in statolith calcium carbonate polymorphs
287 and differences in the crystal structure. Figure 3 shows five stacked intensity traces from
288 sample spots taken within a single statolith (every 20th sample along the growth axis from left

289 to right from a total of 110) overlaid with the intensity trace for calcite and aragonite. None
290 of the sample peaks corresponded to the characteristic peaks for calcite; instead all five
291 sample spots were identified as aragonite. This was also found in the other 105 samples from
292 this specimen. μ XRD was used to analyse mineralogical composition and crystallographic
293 properties (crystal structure) of each of the 18 statoliths. Regardless of sample origin or whelk
294 gender, no calcite was identified and all were shown to be aragonite. A 120 second exposure
295 to the X-ray beam at both the outer edge and centre of a single statolith caused no changes
296 in the diffraction peaks indicating that the X-ray beam had not damaged the samples
297 crystallographically during analysis (see supplementary material, SMFigure 1). μ XRD traces
298 acquired from broken, unprocessed statoliths showed a diffraction pattern identical to that
299 of the processed statoliths (SMFigure 2), indicating no crystallographic change had occurred
300 during sample preparation.

301 The crystal structure of each statolith changed along the growth axes, the intensity of a range
302 of aragonite-specific diffraction peaks changed across the sample, this can be observed for
303 (a) field-collected and (b) laboratory reared (Menai Strait) whelk statoliths (Figure 4). The
304 number of high-intensity peaks increased with proximity to the central nucleus. However, all
305 peaks were present in almost all XRD patterns from every sample, but they were often
306 obscured by a highly intense peak towards the statolith outer edge. SEM of mounted broken
307 statoliths revealed a crystal orientation radiating from the central nucleus, giving a clear
308 hourglass-shaped appearance of the microstructure in the exposed surfaces of the broken
309 statolith (Figure 5).

310 3.2. *Statolith chemistry*

311 Trace elemental profiles of three representative statoliths from each site are shown in Figure
312 6, a summary table of the elemental ratios for each site can be seen in Table 1. Whilst several
313 trace elements were analysed with SIMS, Mg/Ca ratios had the clearest cycles with minima
314 corresponding to the dark annual growth rings (i.e. observed winter minimum in the seawater
315 temperature cycle (Hollyman *et al.*, 2017)). Although the overall Mg/Ca ratios were 10-15
316 times lower than those of Na/Ca and Sr/Ca (Table 1), this seasonal pattern was consistently
317 observed in all sampled specimens. Sr/Ca ratios displayed some cycles with similar patterns
318 of minima corresponding to the growth rings but these were inconsistent and in places were
319 anti-correlated. The Sr/Ca ratios in all adult statoliths displayed an ontogenetic increase
320 towards the outer statolith edge. This was confirmed using ANOVA, at each site a significant
321 difference was found between the compiled outer 10 sample spots from each statolith with
322 the compiled 10 central sample spots (Jersey – $p < 0.005$, $F = 21.5$; Menai Strait – $p < 0.005$, F
323 $= 17.93$; Shetland – $p < 0.005$, $F = 25.2$). Cycles of Na/Ca ratios in each statolith displayed clear
324 inverse correlations with the Mg/Ca ratio profiles, and all showed a characteristic rise towards
325 the right hand edge of the statolith ending the profile ~ 4 mmol/mol higher than in the centre
326 of the statolith. This was observed in all 18 of the adult whelk statoliths and 6 of the 12
327 juvenile whelk statoliths analysed.

328 The peak of the second Mg/Ca cycle in each statolith was markedly lower than that of the first
329 cycle peak, this was common to all samples. To investigate a likely annual periodicity in the
330 Mg cycles, statoliths from laboratory reared animals of known age (one and two years) were
331 analysed. Mg/Ca profiles from statoliths of juvenile whelks, two one-year-old animals of
332 varying size (a & b) and two two-year-old animals of varying size (c & d) are shown in Figure
333 7. The one-year-old specimens have one single Mg/Ca ratio peak beyond the hatching ring,

334 irrespective of size. The two-year-old specimens have two cycles beyond the hatching ring
335 again irrespective of size, with the amplitude of the second cycle being markedly lower than
336 the first. A lower amplitude peak in the second Mg/Ca cycle was also observed in all the field-
337 collected whelk statoliths, irrespective of location or gender, making this pattern identical in
338 field-collected and laboratory reared specimens. The first Mg/Ca peak in the Menai Strait
339 statoliths was visibly higher than those from the Shetland Isles. However, the peak in the
340 second Mg/Ca cycle from the Menai Strait and the Shetland Isles statoliths were similar, whilst
341 statoliths collected from Jersey had a visibly higher second Mg/Ca cycle. Average summer
342 maximum temperatures over the study period differed between sites with Shetland as the
343 coldest ($14.1^{\circ}\text{C} \pm 0.7$), followed by the Menai Strait ($17.8^{\circ}\text{C} \pm 0.2$) and Jersey ($18.6^{\circ}\text{C} \pm 0.3$)
344 which were much more similar. Significant differences in the peak heights of the Mg cycles
345 (excluding the exaggerated first year peak) between sites were found using ANOVA ($F =$
346 21.538 , $p < 0.001$). Post-hoc Tukey's test revealed significantly higher Mg/Ca ratio peaks in
347 the Jersey statoliths than either of the Menai Strait and Shetland Isles statoliths, with the
348 Menai Strait statoliths having a significantly higher Mg /Ca ratio than the Shetland Isles. These
349 findings, summarised in Table 1, potentially indicate temperature related site differences and
350 control of Mg incorporation into the statoliths.

351 The relationships between the different Na/Ca and Mg/Ca ratios in statoliths from male and
352 female *B. undatum* are shown in Figure 8. The element ratios in the central portion of each
353 statolith (within the hatching ring) were not included in the correlations as the intensity in the
354 SIMS analyses was irregular and inconsistent compared with the subsequent juvenile and
355 adult growth (see SMFigure 3). There are clear variations in the elemental relationships in
356 statoliths from whelks both between and within sites, e.g. Na/Ca - Mg/Ca were negatively

357 related and varied within sites. This variation appears to relate to the ratios of Na/Ca rather
358 than Mg/Ca in the statoliths and is likely due to increases in Na towards the edges of each
359 statolith. However, much weaker relationships exist between Sr/Ca - Mg/Ca and Na/Ca –
360 Sr/Ca with both positive and negative relationships between elemental comparisons among
361 sites and within a single site (see supplementary material in SMTTable 1).

362 Direct comparisons of Mg/Ca profiles with seawater temperature highlighted the high degree
363 of variability and physiological control of elemental incorporation. Figure 9 presents Mg/Ca
364 data from a single representative statolith overlaid on the corresponding seawater
365 temperature profile for each site. Mg/Ca data from the first year of growth was removed as
366 this was elevated (Figures 6 & 7), making visual comparison difficult. Average Mg/Ca profiles
367 for each site could not be calculated due to intra-site variability (visible in Figure 8), meaning
368 only data from a single representative statolith is presented. The annual cycles in the Jersey
369 and Menai Strait data are clearly visible (Figure 9 b & c) whereas they are reduced in the
370 Shetland data (Figure 9a; although they are visible when the y-axis maximum is reduced). The
371 reduction in the Mg/Ca data from Shetland (Figure 9a) is clearly disproportionate to the sites
372 lower seawater temperature when compared to Jersey or the Menai Strait. There is also a
373 clear decrease in amplitude in the annual cycles from the Menai Strait, meaning that the full
374 temperature range is likely not recorded by the Mg/Ca profile. The combination of the
375 elevated first year values, high intra-site variability and reductions in cycle amplitude with
376 ontogeny makes the reconstruction of seawater temperature from Mg/Ca data unlikely,
377 limiting their potential as environmental recorders.

378 A visual comparison of changes in diffraction patterns and elemental profiles across each
379 statolith did not reveal any obvious relationships between the two analyses. This was

380 achieved by overlaying the changes in diffraction peak intensities (Figure 4) with the
381 corresponding trace element to calcium profiles (Figures 6 & 7). The statoliths used in Figure
382 4a and b to show the changes in diffraction peaks were also used to present the elemental
383 data in Figures 6b and 7a respectively, there is no visual correlation between these datasets.
384 A figure of the compiled elemental and diffraction data can be found in SMFigure 4.

385 **4. Discussion**

386 The results from this study represent a novel analysis of the crystallography, microstructure
387 and composition of *Buccinum undatum* statoliths using a combination of observations
388 coupled with high precision, cutting-edge techniques. The data obtained from these analyses
389 were used to geochemically validate the annual periodicity of statolith growth ring formation
390 and begin to decipher the controlling factors behind trace element incorporation into
391 gastropod statoliths from whelks of different gender, size and development phases. The
392 results presented here highlight the suitability of techniques such as SIMS and μ XRD for
393 analysing these small structures.

394 4.1. *Statolith crystallography and microstructure*

395 Detailed structural analysis of 18 whole statoliths using μ XRD at 2 μ m resolution confirmed
396 that the statoliths are wholly composed of aragonite with no trace of calcite. Galante-Oliveira
397 *et al.* (2014) concluded that the statoliths of the netted whelk, *Nassarius reticulatus*, were
398 composed of aragonite but they also suspected that a small fraction of calcite was present.
399 However, this was based on a much smaller number of samples ($n = 2$). The XRD patterns
400 presented in Figure 3 never fully resemble that of the speleothem aragonite standard
401 presented in the same figure. This is due to the differing analysis of the two compounds, the

402 standard was analysed with a continuous raster of a powdered sample to maximise the
403 number of aragonite crystal orientations, resulting in many different peaks. The statoliths
404 were analysed with only a single 2 x 2 μm transmission spot which was taken at each point
405 across the statolith, when 'stacked' together, the ~ 100 XRD profiles from each statolith show
406 a much closer resemblance to the aragonite standard (SMFigure 5). Our μXRD analysis
407 indicated that the statoliths had differing structures between the outer edge and centre of
408 each statolith. This was later confirmed using SEM to be observable as an 'hour glass'
409 microstructure. This is potentially why the statoliths are not perfectly spherical but instead
410 are dorso-ventrally flattened. A similar observation in the microstructure was found by
411 Galante-Oliveira *et al.* (2014) in *N. reticulatus* statoliths. The changing XRD spectra across the
412 statoliths (Figure 4), is likely accounted for by the 'hour glass' structure and the thin statolith
413 sections themselves. Figure 10 shows this in more detail, illustrating how a seemingly more
414 complex crystal structure was found in the centre of each statolith as more crystal
415 orientations were available closer to the centre of the sample. X-rays (green arrows in Figure
416 10) passing through close to the centre of the thin section would encounter more crystal
417 orientations than those X-rays passing through the outer edge, this is likely an example of
418 preferred orientation. This is a crystallographic phenomenon resulting in deviations of XRD
419 spectra from known spectra due to 'preferred' orientation of the crystal units in a crystalline
420 material (Hammond, 2015). This reduces the number of lattice planes represented in the
421 spectra (as was seen in the statolith XRD analyses) when compared to the spectra obtained
422 from a well-mixed 'random' powder sample. Whilst highlighting changes in structure across
423 the statolith, these changes in peak intensity showed no apparent correlation to the
424 elemental profiles obtained during SIMS analysis. The lack of obvious changes in peak
425 intensity (and therefore crystallography) corresponding to the visible growth rings indicates

426 that the perturbations responsible for the growth rings do not change the complexity of the
427 crystal structure, and are possibly due to some other factor such as changes in organic matter
428 composition.

429 4.2. SIMS analysis

430 Published accounts of the chemical analyses of molluscan statoliths have frequently focussed
431 on cephalopods (e.g. cuttlefish [Zumholz *et al.*, 2007a; Gillanders *et al.*, 2013] squid [Arkhipkin
432 *et al.*, 2004; Zumholz *et al.*, 2007b; Arbuckle & Wormuth, 2014] and octopods [Ikeda *et al.*,
433 1999]) as opposed to gastropods. However, the results presented here indicate that the
434 chemical composition of *B. undatum* statoliths is comparable to these species groups. Sr/Ca
435 in the statoliths of *B. undatum* (~8 - 12 mmol/mol) falls within the range of reported ratios for
436 cephalopod statoliths (~7 – 28 mmol/mol, e.g. Ikeda *et al.*, 1999; Ikeda *et al.*, 2003 and
437 Gillanders *et al.*, 2013). However, these ratios are higher than those found in fish otoliths (~2
438 – 2.5 mmol/mol, Campana, 1999; ~3 – 4 mmol/mol, Sturrock *et al.*, 2015) and aragonitic
439 mollusc shells (~1.25 – 3.5 mmol/mol, Palacios *et al.*, 1994; ~1 – 3 mmol/mol, Gillikin *et al.*,
440 2005; ~1 – 3 mmol/mol Sosdian *et al.*, 2006). Galante-Oliveira *et al.* (2015) reported periodic
441 changes in the Sr/Ca ratio of statoliths from, the gastropod *N. reticulatus* with maximum
442 concentrations coinciding with winter deposited statolith growth rings in 92% of cases (n =
443 20), suggesting an inverse relationship with seawater temperature. Similarly, Zacherl *et al.*
444 (2003) also reported an inverse correlation between Sr and seawater temperature in the
445 larval statoliths of the marine gastropod *Kelletia kelletii*. However, such relationships were
446 not found in the pre-hatching (larval) area of the statoliths of *B. undatum*, and no clear
447 periodic cycles in the Sr/Ca ratio profiles were seen. The incorporation of Sr into *B. undatum*
448 statoliths is likely to be under greater physiological control than other elements analysed,

449 with some statoliths showing weak seasonal cycles which approximately matched the Mg
450 cycles and growth ring formation. However, Sr cycles were often unclear with extra cycles of
451 Sr apparent when compared with the number of growth rings.

452 One of the striking features of the Sr/Ca ratio cycles observed in all adult statoliths was a clear
453 ontogenetic increase towards the outer edge of the statoliths, this was similar for both male
454 and female whelks from all sampled sites. Laboratory reared specimens showed lower mean
455 values of Sr/Ca when compared to the field-collected specimens. This apparent lack of any
456 ontogenetic trend in Sr/Ca ratio of the laboratory reared animals can be accounted for by age,
457 as the laboratory reared specimens were juveniles (one and two-years-old) whereas the field-
458 collected specimens were 4+ years old. However, on average the two-year-old whelk
459 statoliths contained higher Sr/Ca values than the one-year-olds, suggesting a possible
460 ontogenetic increase in Sr/Ca ratios in the laboratory reared whelk statoliths as well.
461 Ontogenetic changes in Sr incorporation are well documented for bivalve and gastropod
462 shells, with several species exhibiting a similar increase with ontogeny (e.g. *Mya arenaria*
463 [Palacios *et al.*, 1994]; *Clavilithes macrospira*, *Venericardia planicosta* [Purton *et al.*, 1999];
464 *Conus ermenius* [Sosdian *et al.*, 2006]). These ontogenetic trends of Sr in mollusc shells are
465 often ascribed to changes in growth rate with age (Palacios *et al.*, 1994; Sosdian *et al.*, 2006),
466 more specifically, changes in metabolic activity associated with age and decreasing growth
467 rate (Purton *et al.*, 1999). Decreasing growth with age has been demonstrated for this species
468 (Shelmerdine *et al.*, 2007; Hollyman, 2017) which may well explain the apparent ontogenetic
469 increase of Sr within the statoliths. Further work should therefore focus on investigating a
470 possible growth rate control over Sr incorporation in gastropod statoliths.

471 Currently only one paper has investigated the presence of Mg in gastropod statoliths. Lloyd
472 *et al.* (2008) reported on the effect of temperature and egg source effects (i.e. the effect of
473 the larval food source and the egg on trace element incorporation) in larval *K. kelletii* enclosed
474 within their egg cases. Conversely, they found no effect of temperature on Mg incorporation
475 although an inverse relationship between Sr and seawater temperature was found. This
476 strong relationship between the concentrations of Mg in the egg source and the statolith
477 suggested a tight control of magnesium incorporation from the food source in this species. In
478 addition to this, the period of larval growth within the egg capsule demonstrated higher
479 concentrations of Mg than during the juvenile growth period. As juvenile *B. undatum* develop
480 directly from the egg capsule and have a similar life cycle to *K. Kelletii*, it is possible that this
481 may be the reason behind the increased Mg/Ca ratio seen in the first annual cycle of each
482 statolith in this study. Mg enrichment in the cores of cephalopod statoliths is also well
483 documented (e.g. *Gonatus fabricii* - Zumholz *et al.*, 2007b; *Doryteuthis opalescens* - Warner
484 *et al.*, 2009), and as such it can be used as a chemical marker to denote the position of the
485 core itself (e.g. *Dosidicus gigas* - Arbuckle & Wormuth, 2014). Zumholz *et al.*, (2006) also
486 found that food source had a strong control on the incorporation of elements such as Sr into
487 the statoliths of the cuttlefish *Sepia officinalis*. They observed elevated levels of Mg in the
488 core of the statoliths. Whilst this is not a direct gastropod example, it does show the potential
489 of a food source to impact upon trace element incorporation within molluscan statoliths.

490 The annual periodicity of statolith growth rings has already been validated for juvenile
491 laboratory reared specimens (see Hollyman *et al.*, 2017) which implies an annual periodicity
492 in the cycles in the Mg/Ca profiles and in the Na/Ca profiles. This was confirmed with the
493 elemental analysis of statoliths from laboratory reared animals of known age. The analysis of

494 statoliths from one and two-year-old animals revealed 1 and 2 Mg cycles respectively, which
495 correspond to the visible annual statolith growth rings. All analysed statolith samples of *B.*
496 *undatum* revealed Mg cycles with minimum values corresponding to the visible dark statolith
497 growth rings (Figures 6 & 7) and therefore a possible positive relationship with SST as these
498 rings are formed in the winter (Hollyman *et al.*, 2017). This is at direct odds with
499 thermodynamic predictions from abiogenic precipitation experiments which found a negative
500 relationship between Mg/Ca and temperature (Gaetani & Cohen, 2006). Several previous
501 studies have presented similar findings with element/Ca ratios at odds with precipitation
502 experiments (e.g. Sosdian *et al.*, 2006 [Sr in the shells of *Conus ermenius*]; Purton *et al.*, 1994
503 [Sr in the shells of *Clavilithes macrospira* and *Venericardia planicosta*). In itself, this fact
504 suggests a high degree of physiological control on the incorporation of Mg into the statoliths.
505 However, clear annual cycles are present between visible growth lines, suggesting the
506 metabolic processes controlling Mg incorporation may be under temperature control. Visual
507 comparison of SST (Sea Surface Temperature) records and statolith Mg/Ca data at each site
508 (Figure 9) shows large inter and intra site variability in element incorporation. This variability
509 along with the elevated Mg/Ca in the first year of life precluded the calculation of a Mg -
510 seawater temperature relationship. This finding suggests that the statoliths of *B. undatum*
511 hold little value as environmental recorders unless more reliable elemental proxies are
512 developed or further work enables the physiological controls to be accounted for. However,
513 seasonal cycles are still clearly evident, allowing an estimation of age from the cycles of Mg.
514 This is similar to the findings of Durham *et al.* (2017), who identified seasonal cycles in Mg/Ca
515 in the shells of *Crassostrea virginica* and *Magallana gigas*, allowing age determination of
516 individual specimens.

517 Several clear patterns in Mg incorporation were evident; firstly, more Mg was incorporated
518 into the statoliths collected from Jersey in comparison to those from the Shetlands. The mean
519 Mg/Ca values at each site increased with decreasing latitude from the coldest site (Shetland)
520 to the warmest (Jersey); this was not proportionate to the SST change with far clearer
521 differences in Mg/Ca between sites than those seen in SST (Figure 9). ANOVA also showed
522 statistical differences between the maximum peak values for Mg between sites. This supports
523 the idea that Mg is positively correlated with temperature as the seawater temperature
524 regimes at each of the three sites clearly differ (Figure 1a) with Shetland being the coldest
525 and Jersey the warmest. Secondly, the maximum of the Mg/Ca ratio peak in the first annual
526 cycle was higher than all subsequent cycles in all statoliths. Whilst this was not as pronounced
527 in some whelks, the innermost cycle was always higher irrespective of the location of the
528 whelks or their gender. Evident in several statoliths, the annual Mg cycles from the oldest
529 whelks were lower in amplitude with ontogeny. This was possibly due to a constraint of
530 sampling resolution resulting in time averaging of portions of the Mg annual cycle between
531 the narrower older growth rings, effectively smoothing out the amplitude of the cycles.
532 Alternatively, this may have been the result of an ontogenetic decrease in growth rate;
533 something that *B. undatum* has been shown to display from ageing studies (Shelmerdine *et*
534 *al.*, 2007; Hollyman, 2017).

535 Considering the seasonal patterns in the Mg profiles (i.e. the cycles match the annual growth
536 rings) along with the elevated incorporation of Mg in the first year of life might suggest a
537 combination of both physiological and thermodynamic controls over Mg incorporation within
538 the statoliths. With physiological controls likely playing a more prominent role within the first

539 year of growth. Further work should focus on disentangling the environmental and
540 physiological controls on trace element incorporation into statoliths.

541 Sodium ratios in many statoliths showed strong and moderate negative relationships with
542 Mg. The stronger negative relationships were more often seen in the Menai Strait and Jersey
543 whelk statoliths. Unlike Mg, no clear pattern of increased Na incorporation was seen in the
544 first annual cycle, although, like Mg in older statoliths, the amplitude of the cycles decreased
545 with age. The incorporation of Na into the statoliths is likely controlled by some factor with
546 an annual cycle such as seasonal seawater temperature or growth rate (which is currently not
547 well established for this species) as the cycles in Na/Ca corresponded with the annual growth
548 rings. However, recent work by Yoshimura *et al.* (2017), suggests that biological and
549 environmental controls of Na incorporation into biogenic carbonates are minimal.
550 Temperature effects on the precipitation of Na in aragonite are unknown. However, Okumura
551 and Kitano (1986) demonstrated that Mg ions in a precipitating fluid are anti-correlated to
552 the precipitation of Na into aragonite in laboratory precipitation experiments, this may be a
553 fundamental control of Na incorporation in this instance. At the right-hand edge of each adult
554 whelk statolith the Na/Ca profiles rose unexpectedly, likely as a result of an edge effect caused
555 by the low incidence angle of the ion beam (30°). It is unclear why Na/Ca ratios were affected
556 when Sr/Ca and Mg/Ca ratios were not.

557 No literature could be found relating to the incorporation of Na into gastropod statoliths,
558 however, Zumholz *et al.* (2007c) found putative daily cycles of Na/Ca in the statoliths of the
559 squid *Gonatus fabricii* using nanoSIMS. It was concluded that these cycles corresponded with
560 daily growth rate changes as a result of a diurnal feeding cycle and were inversely correlated
561 to Sr/Ca ratios. The findings from this study and those of Zumholz *et al.* (2007c) have

562 demonstrated and confirmed the suitability of high sensitivity, high resolution techniques
563 such as SIMS and nanoSIMS for studying the geochemistry of small biogenic carbonate
564 structures.

565 5. Conclusion

566 The growth rings within *B. undatum* statoliths were found to contain clear, negatively
567 correlated cycles in Mg and Na at all three sites and within laboratory reared animals, likely
568 controlled by a combination of environmental and physiological factors. This supports the
569 conclusion of Hollyman *et al.* (2017), suggesting that the growth rings have a clear annual
570 periodicity. The cycles in Sr also displayed an ontogenetic increase, something which has
571 never been uncovered at sub-annual resolution in gastropod statoliths. The clear variation
572 and possible physiological controls over element incorporation makes the prospect of
573 environmental reconstructions from these structures unfeasible. This geochemical validation
574 of growth line formation periodicity will allow fisheries scientists to confidently use *B.*
575 *undatum* statoliths for age determination within a fisheries monitoring context. This adds a
576 much-needed tool to monitoring programs for this species in areas where it is of commercial
577 importance.

578 6. Acknowledgements

579 This work was supported through a Bangor University/CEFAS partnership PhD scholarship to
580 P.R.H. We are grateful to Berwyn Roberts for collection of whelk egg cases, Gwynne Parry-
581 Jones for sample collection from the Menai Strait, Mark Hamilton (NAFC) for sample
582 collection from Shetland and Jon Shrives (DoE Jersey) for sample collection from Jersey. All
583 SIMS analysis was undertaken through a facility grant application (IMF543/1114) with

584 continuing help and advice from Drs Richard Hinton and John Craven, post-visit. Access to the
585 Diamond Light Source for XRD analysis was granted through a rapid access facility grant
586 application (sp13616-1). We also thank Drs Lorraine Field and Andy Marriott (BGS) for their
587 help with the SEM imaging. And again to Andy Marriott for his helpful comments on this
588 manuscript. We also thank the two anonymous reviewers and the editor for their helpful
589 comments to improve this manuscript.

590 7. References

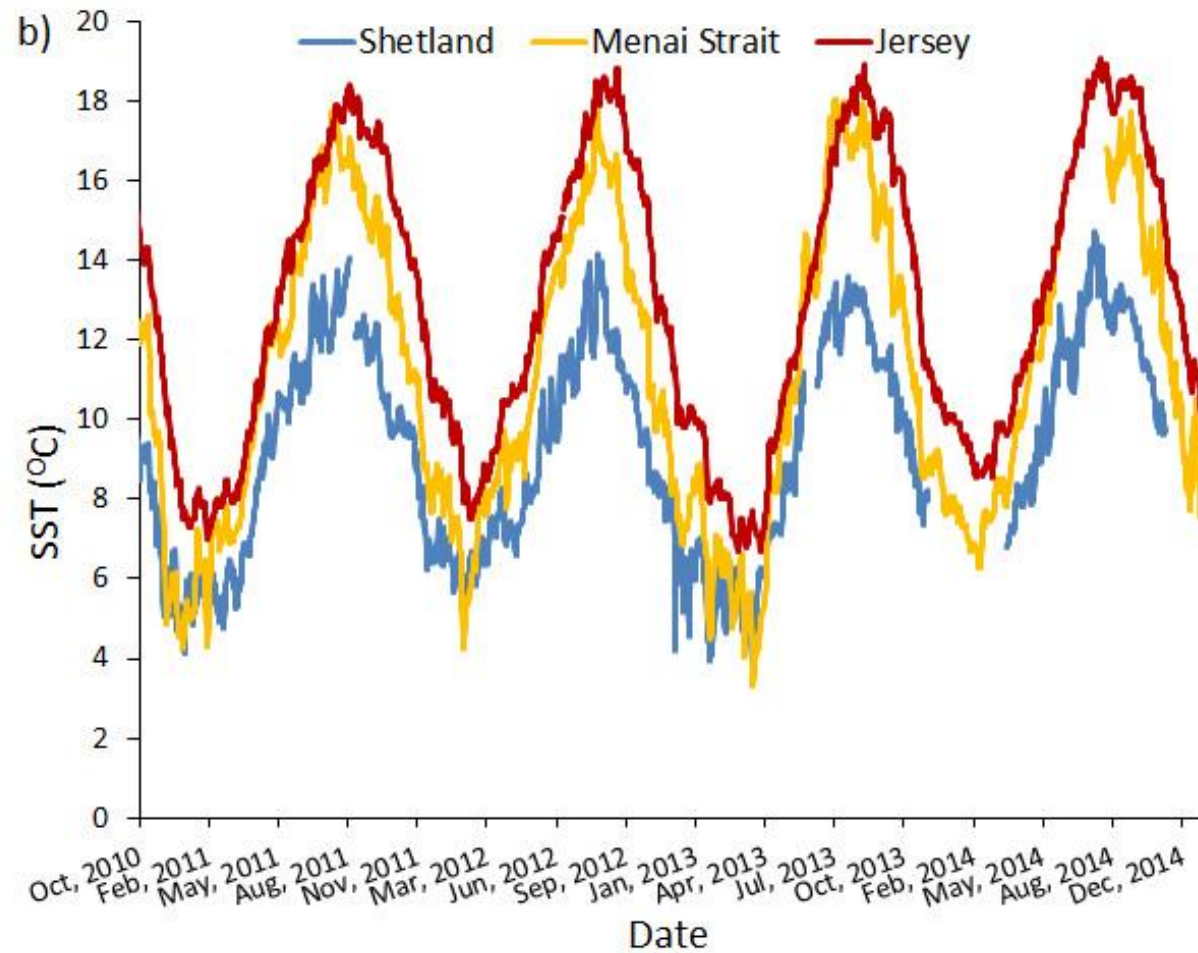
- 591 Arbutckle NSM, Wormuth JH (2014) Trace elemental patterns in Humboldt squid statoliths from three
592 geographic regions. *Hydrobiologia* 725:115–123
- 593 Arkhipkin AI (2005) Statoliths as ‘black boxes’ (life recorders) in squid. *Mar Freshw Res* 56: 573–583
- 594 Arkhipkin AI, Campana SE, FitzGerald J, Thorrold SR (2004) Spatial and temporal variation in elemental
595 signatures of statoliths from the Patagonian longfin squid (*Loligo gahi*). *Can J Fish Aquat Sci* 61:1212–
596 1224
- 597 Barroso CM, Nunes, M, Richardson CA, Moreira MH (2005) The gastropod statolith: a tool for
598 determining the age of *Nassarius reticulatus*. *Mar Biol* 146: 1139–1144
- 599 Basham M, Filik J, Wharmby MT, Chang PCY, Kassaby BE, Gerring M, Aishima J, Levik K, Pulford BCA,
600 Sikharulidze I, Sneddon D, Webber M, Dhesi SS, Maccherozzi F, Svensson O, Brockhauser S, Nárayc G,
601 Ashton AW (2015) Data Analysis WorkbeNch (DAWN) *J Synchrotron Rad* 22:853-858
- 602 Bice KL, Layne GD, Dahl K (2005) Application of secondary ion mass spectrometry to the
603 determination of Mg/ Ca in rare, delicate, or altered planktonic foraminifera: examples from the
604 Holocene, Paleogene, and Cretaceous. *Geochem Geophys Geosyst* 6:Q12P07
- 605 Billings GK, Ragland PC (1968) Geochemistry and mineralogy of the recent reef and lagoonal
606 sediments south of Belize (British Honduras). *Chem Geol* 3:135–153
- 607 Brinza L, Schofield PF, Mosselmans JFW, Donner E, Lombi E, Paterson D, Hodson ME (2014) Can
608 earthworm-secreted calcium carbonate immobilise Zn in contaminated soils? *Soil Biol Biochem* 74:1-
609 10
- 610 Campana SE (1999) Chemistry and composition of fish otoliths: pathways, mechanisms and
611 applications. *Mar Ecol Prog Ser* 188:263–297
- 612 Chase R (2002) Behaviour and its neural control in gastropod molluscs. Oxford University Press, New
613 York, NY

- 614 Chatzinikolaou E, Richardson CA (2007) Evaluating growth and age of netted whelk *Nassarius*
615 *reticulatus* (Gastropoda: Nassariidae) using statolith growth rings. Mar Ecol Prog Ser 342:163-176
- 616 Dietzel M, Gussone N, Eisenhauer A (2004) Co-precipitation of Sr²⁺ and Ba²⁺ with aragonite by
617 membrane diffusion of CO₂ between 10 and 50°C. Chem Geol 203:139–151
- 618 Dodd JR (1965) Environmental control of strontium and magnesium in *Mytilus*. Geochim Cosmochim
619 Acta 29:385-398
- 620 Durham SR, Gillikin DP, Goodwin DH, Dietl GP (2017) Rapid determination of oyster lifespans and
621 growth rates using LA-ICP-MS line scans of Mg/Ca ratios. Palaeogeogr Palaeoclim Palaeoecol *In Press*
622 <https://doi.org/10.1016/j.palaeo.2017.06.013>
- 623 Freitas P, Clarke LJ, Kennedy H, Richardson C, Abrantes F (2005) Mg/Ca, Sr/Ca, and stable-isotope ($\delta^{18}\text{O}$
624 and $\delta^{13}\text{C}$) ratio profiles from the fan mussel *Pinna nobilis*: seasonal records and temperature
625 relationships. Geochem Geophys Geosyst 6:Q04D14
- 626 Gaetani GA, Cohen AL (2006) Element partitioning during precipitation of aragonite from seawater: A
627 framework for understanding paleoproxies. Geochim Cosmochim Acta 70:4617-4634
- 628 Galante-Oliveira S, Marçal R, Espadilha F, Sá M, Abell R, Machado J, Barroso C (2015) Detection of
629 periodic Sr Ca⁻¹ cycles along gastropod statoliths allows the accurate estimation of age. Mar Biol
630 162:1473-1483
- 631 Galante-Oliveira S, Marçal R, Guimarães F, Soares J, Lopes JC, Machado J, Barroso CM (2014)
632 Crystallinity and microchemistry of *Nassarius reticulatus* (Caenogastropoda) statoliths: towards their
633 structure stability and homogeneity. J Struct Biol 186:292–301
- 634 Gentry DK, Sosdian S, Grossman EL, Rosenthal Y, Hicks D, Lear CH (2008) Stable isotope and Sr/Ca
635 profiles from the marine gastropod *Conus ermineus*: testing a multiproxy approach for inferring
636 paleotemperature and Paleosalinity. Palaios 23:195-209
- 637 Gillanders BM, Wilkinson LM, Munro AR, de Vries MC (2013) Statolith chemistry of two life history
638 stages of cuttlefish: Effects of temperature and seawater trace element concentration. Geochim
639 Cosmochim Acta 101:12-23
- 640 Gillikin DP, Lorrain A, Navez J, Taylor JW, André L, Keppens E, Baeyens W, Dehairs F (2005) Strong
641 biological controls on Sr/Ca ratios in aragonitic marine bivalve shells. Geochem Geophys Geosyst
642 6:Q05009
- 643 Gong YUT, Killian CE, Olson IC, Appathurai NP, Amasino AL, Martin MC, Holt LJ, Wilt FH, Gilbert PUPA
644 (2012) Phase transitions in biogenic amorphous calcium carbonate. P Natl Acad Sci USA 109(16):6088-
645 6093
- 646 Haig JA, Pantin, JR, Murray LG, Kaiser MJ (2015) Temporal and spatial variation in size at maturity of
647 the common whelk (*Buccinum undatum*). ICES J Mar Sci 72 (9):2707-2719
- 648 Hammond C (2015) The basics of crystallography and diffraction, fourth edition. International union
649 of crystallography, Oxford University press, Oxford, UK, 542 pp.

- 650 Hollyman PR (2017) Age, growth and reproductive assessment of the whelk, *Buccinum undatum*, in
651 coastal shelf seas. Unpublished PhD thesis, Bangor University. 404 pp.
- 652 Hollyman PR, Leng MJ, Chenery SRN, Laptikhovsky VV, Richardson CA (2017) Statoliths of the whelk
653 *Buccinum undatum*: a novel age determination tool. Mar Ecol Prog Ser. doi: 10.3354/meps12119
- 654 Ikeda Y, Arai N, Kidokoro H, Sakamoto W (2003) Strontium: calcium ratios in statoliths of Japanese
655 common squid *Todarodes pacificus* (Cephalopoda: Ommastrephidae) as indicators of migratory
656 behaviour. Mar Ecol Prog Ser 251:169–179
- 657 Ikeda Y, Arai N, Sakamoto W, Mitsuhashi M, Yoshida K (1999) Preliminary report on PIXE analysis for
658 trace elements of *Octopus dofleini* statoliths. Fish Sci 65:161–162
- 659 Kasemann SS, Schmidt DN, Bijma J, Foster GL (2009) In situ boron isotope analysis in marine
660 carbonates and its application for foraminifera and palaeo-pH. Chem Geol 260:138–147
- 661 Katz A (1973) The interaction of magnesium with calcite during crystal growth at 25-90°C and one
662 atmosphere. Geochim Cosmochim Acta, 37:1563-1586
- 663 Kinsman DJJ, Holland HD (1969) The co-precipitation of cations with CaCO₃-IV. The co-precipitation of
664 Sr²⁺ with aragonite between 16° and 96°C. Geochim Cosmochim Acta 33:1-17
- 665 Klein RT, Lohmann KC, Thayer CW (1996) Sr/Ca and 13C/12C ratios in skeletal calcite of *Mytilus*
666 *trossulus*: Covariation with metabolic rate, salinity, and carbon isotopic composition of seawater.
667 Geochim Cosmochim Acta 604:207-4221
- 668 Lloyd DC, Zacherl DC, Walker S, Paradis G, Sheehy M, Warner RR (2008) Egg source, temperature and
669 culture seawater affect elemental signatures in *Kelletia kelletii* larval statoliths. Mar Ecol Prog Ser
670 353:115–130
- 671 Lombarte A, Rufino MM, Sánchez P (2006) Statolith identification of Mediterranean Octopodidae,
672 Sepiidae, Loliginidae, Ommastrephidae and Enoploteuthidae based on warp analysis. J Mar Biol Assoc
673 UK 86:767–771
- 674 McIntyre R, Lawler A, Masfield R (2015) Size of maturity of the common whelk, *Buccinum undatum*:
675 Is the minimum landing size in England too low? Fish Res 162:53–57
- 676 Department for Environment, Food & Rural affairs, Fisheries statistics unit (2004). United Kingdom
677 Sea Fisheries statistics, 2003. Office for National Statistics, London
- 678 Marine Management Organisation (2016) UK Sea Fisheries Statistics 2015. Office for National
679 Statistics, London
- 680 Mooney CJ, Kingsford MJ (2017) Discriminating populations of medusae (*Chironex fleckeri*, Cubozoa)
681 using statolith microchemistry. Mar Freshwater Res 68:1144-1152
- 682 Mucci A (1987) Influence of temperature on the composition of magnesian calcite overgrowths
683 precipitated from seawater. Geochim Cosmochim Acta 51:1977-1984

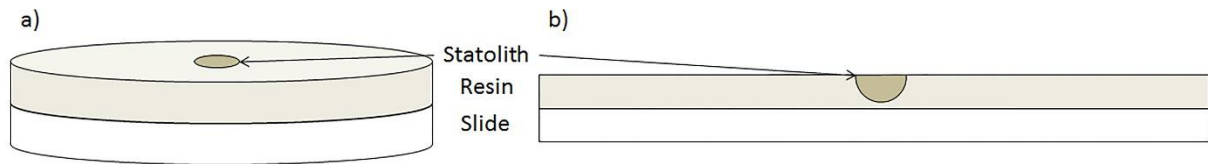
- 684 Nehrke G, Poigner H, Wilhelms-Dick D, Brey T, Abele D (2012) Coexistence of three calcium carbonate
685 polymorphs in the shell of the Antarctic clam *Laternula elliptica*. *Geochem Geophys Geosyst* 13(5):1-
686 8
- 687 Okumura M, Kitano Y (1986) Coprecipitation of alkali metal ions with calcium carbonate. *Geochim*
688 *Cosmochim Acta* 50:49–58
- 689 Palacios R, Orensanz JM, Armstrong DA (1994) Seasonal and life-long variation of Sr/Ca ratio in shells
690 of *Mya arenaria* from Grays Harbor (Washington)—An ancillary criterion in demographic studies.
691 *Estuar Coast Shelf Sci* 39:313–327
- 692 Purton LMA, Shields GA, Brasier MD, Grime GW (1999) Metabolism controls Sr/Ca ratios in fossil
693 aragonitic mollusks. *Geology* 27:1083–1086
- 694 Radha AV, Forbes TZ, Killian CE, Gilbert PUPA, Navrotsky A (2010) Transformation and crystallization
695 energetics of synthetic and biogenic amorphous calcium carbonate. *PNAS* 107(38):16438–16443
- 696 Richardson CA (2001) Molluscs as archives of environmental change. *Oceanogr Mar Biol* 39:103–164
- 697 Richardson CA, Kingsley-Smith PR, Seed R, Chatzinikolau E (2005) Age and growth of the naticid
698 gastropod *Polinices pulchellus* (Gastropoda: Naticidae) based on length frequency analysis and
699 statolith growth rings. *Mar Biol* 148:319–326
- 700 Schöne BR, Zhang Z, Jacob D, Gillikin DP, Tütken T, Garbe-Schönberg D, McConnaughey T, Soldati A
701 (2010) Effect of organic matrices on the determination of the trace element chemistry (Mg, Sr, Mg/Ca,
702 Sr/Ca) of aragonitic bivalve shells (*Arctica islandica*) – Comparison of ICP-OES and LA-ICP-MS data.
703 *Geochem J* 44:23-37
- 704 Shelmerdine RL, Adamson J, Laurenson CH, Leslie B (2007) Size variation of the common whelk,
705 *Buccinum undatum*, over large and small spatial scales: Potential implications for micro-management
706 within the fishery. *Fish Res* 86:201-206
- 707 Sosdian S, Gentry DK, Lear CH, Grossman EL, Hicks D, Rosenthal Y (2006) Strontium to calcium ratios
708 in the marine gastropod *Conus ermineus*: growth rate effects and temperature calibration. *Geochem*
709 *Geophys* 7(11):1525-2027
- 710 Speer JA (1983) Crystal chemistry and phase relations of the orthorhombic carbonates. *Rev Mineral*
711 *Geochem* 11:145–190
- 712 Sturrock AM, Hunter E, Milton JA, EIMF, Johnson RC, Waring CP, Trueman CN (2015) Quantifying
713 physiological influences on otolith microchemistry. *Methods Ecol Evol* 6:806–816
- 714 Warner RR, Hamilton SL, Sheehy MS, Zeidberg LD, Brady BC & Caselle JE (2009) Geographic variation
715 in natal and early larval trace-elemental signatures in the statoliths of the market squid *Doryteuthis*
716 (formerly *Loligo*) *opalescens*. *Mar Ecol Prog Ser* 379:109–121
- 717 Yan H, Shao D, Yuhong W, Sun L (2013) Sr/Ca profile of long-lived *Tridacna gigas* bivalves from South
718 China Sea: a new high-resolution SST proxy. *Geochim Cosmochim Acta* 112:52-65
- 719 Yoshimura T, Tamenori Y, Suzuki A, Kawahata H, Iwasaki N, Hasegawa H, Nguyen LT, Kuroyanagi A,
720 Yamazaki T, Kuroda J, Ohkouchi N (2017) Altrivalent substitution of sodium for calcium in biogenic

- 721 calcite and aragonite. *Geochim Cosmochim Acta* 202:21-38
- 722 Zacherl DC, Paradis G, Lea D (2003) Ba and Sr uptake into larval protoconchs and statoliths of the
723 marine neogastropod *Kelletia kelletii*. *Geochim Cosmochim Acta* 67:4091–4099
- 724 Zumholz K, Hansteen T, Hillion F, Horreard F, Piatkowski U (2007c) Elemental distribution in
725 cephalopod statoliths: NanoSIMS provides new insights into nano-scale structure. *Rev Fish Biol*
726 *Fisheries* 17:487–491
- 727 Zumholz K, Hansteen TH, Klügel A, Piatkowski U (2006) Food effects on statolith composition of the
728 common cuttlefish (*Sepia officinalis*). *Mar Biol* 150:237–244
- 729 Zumholz K, Hansteen TH, Piatkowski U, Croot PL (2007a) Influence of temperature and salinity on the
730 trace element incorporation into statoliths of the common cuttlefish (*Sepia officinalis*). *Mar Biol*
731 151:1321–1330
- 732 Zumholz K, Klügel A, Hansteen T, Piatkowski U (2007b) Statolith microchemistry traces the
733 environmental history of the boreoatlantic armhook squid *Gonatus fabricii*. *Mar Ecol Prog Ser*
734 333:195–204



735
736
737
738

Figure 1a) A map of the United Kingdom showing the three sampling locations (black stars). b) Daily recorded seasonal sea surface temperature (SST) records between October 2010 and February 2014 from the three main study sites. Gaps in the Shetland and Menai Strait temperature data were due to temperature logger failures. Data were obtained from Marine Scotland (Shetland), Department of the Environment (Jersey) and CEFAS (Menai Strait).



739

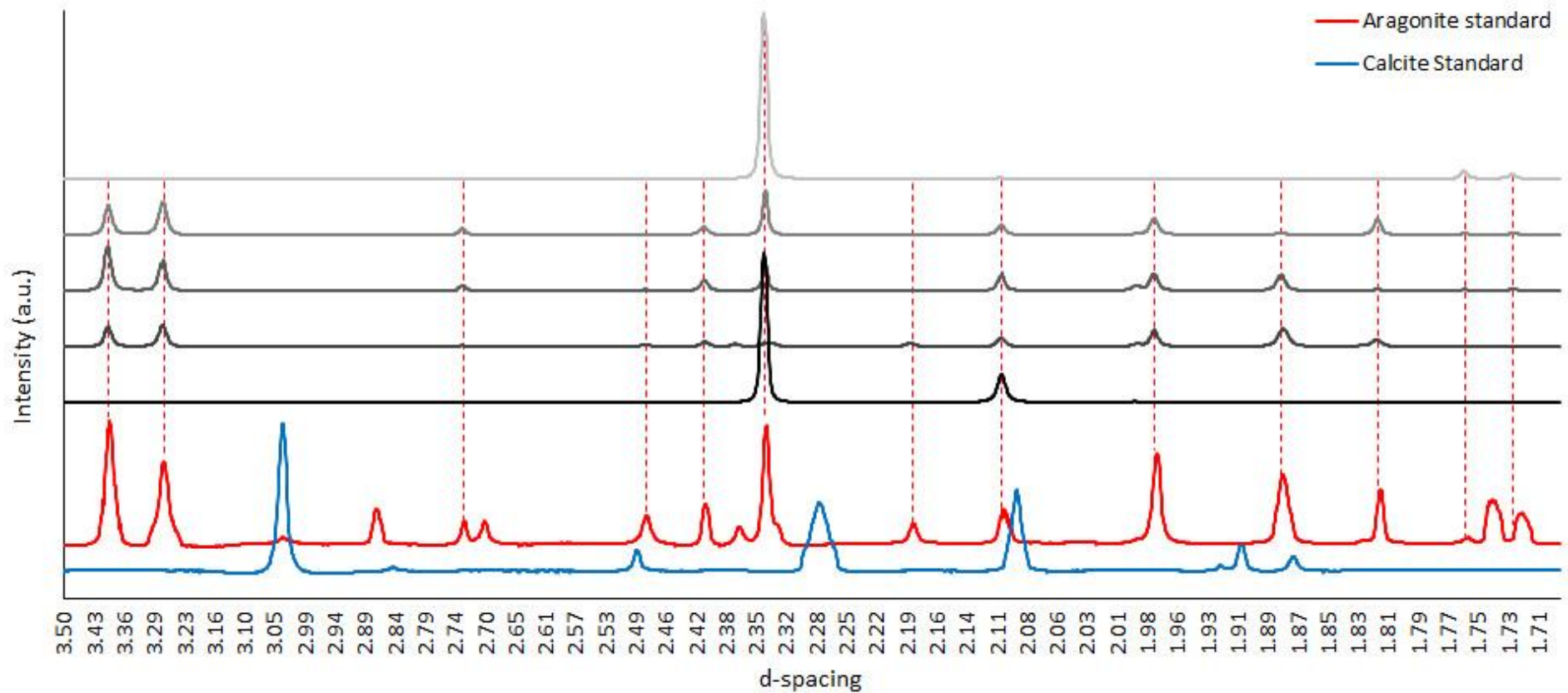
740

741

742

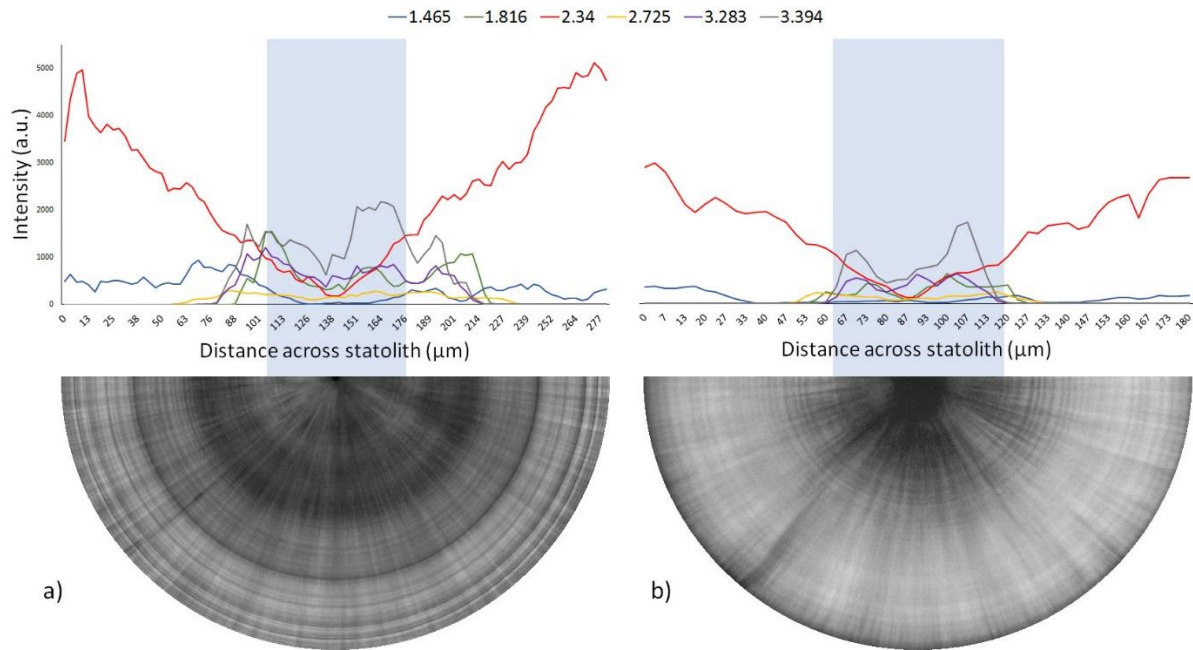
743

Figure 2. Diagrammatic representation of an embedded statolith used in the SIMS analysis. (a) Represents a statolith placed in the centre of a circular glass slide and (b) shows a lateral view of a cross section through the statolith centre. The statoliths have been enlarged in these diagrams for visibility, representing a diameter of roughly 2 mm as opposed to an actual size of ~ 0.25 mm.



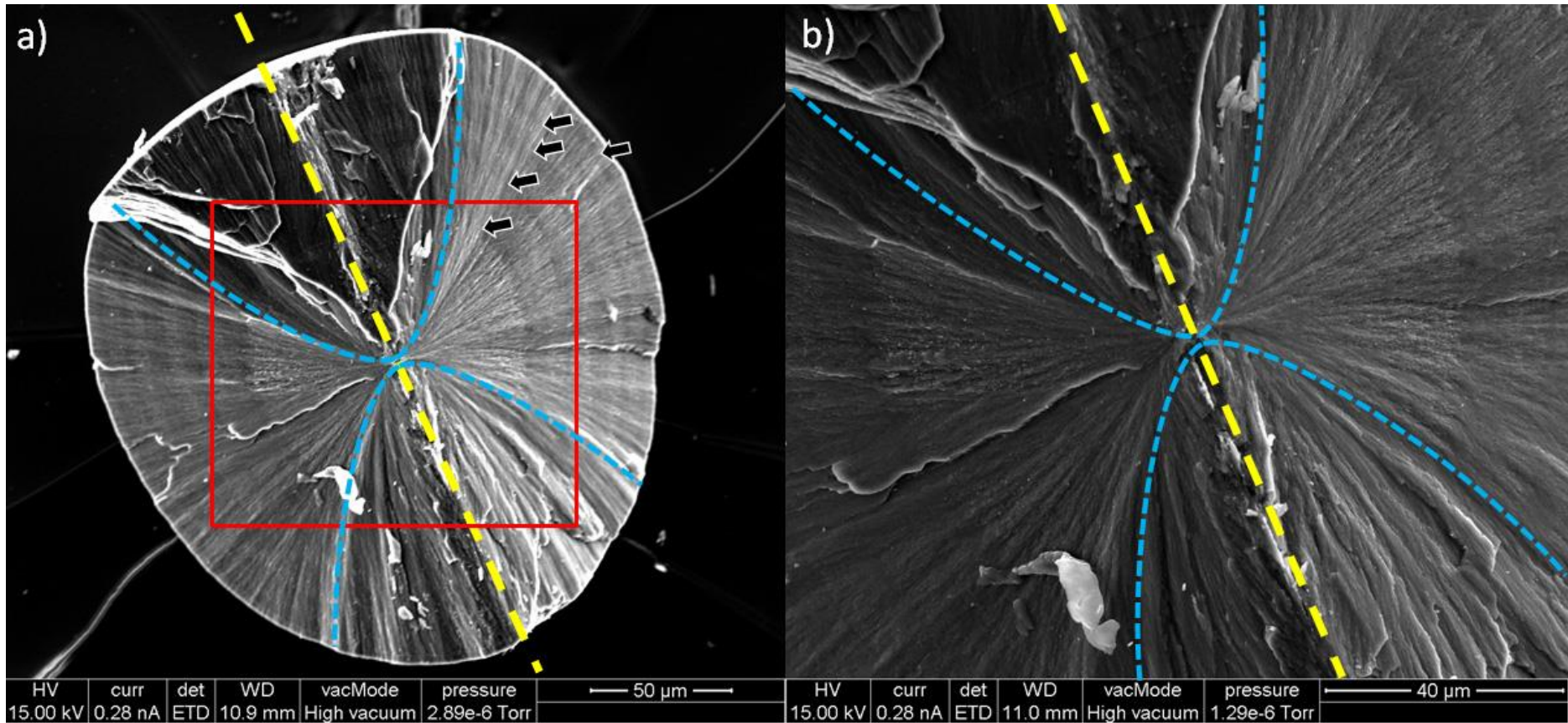
744

745 Figure 3. A stacked plot of 5 diffraction patterns taken from a line profile across the centre of a single sectioned *Buccinum undatum* statolith (every 20th profile from a total
 746 of 110, black and grey lines). The traces from the calcite standard (blue line) and aragonite standard (red line) are overlaid for comparison. Red dotted lines represent
 747 congruent peaks between the aragonite standard and the statolith sample. Y-axes are presented arbitrary units of intensity.

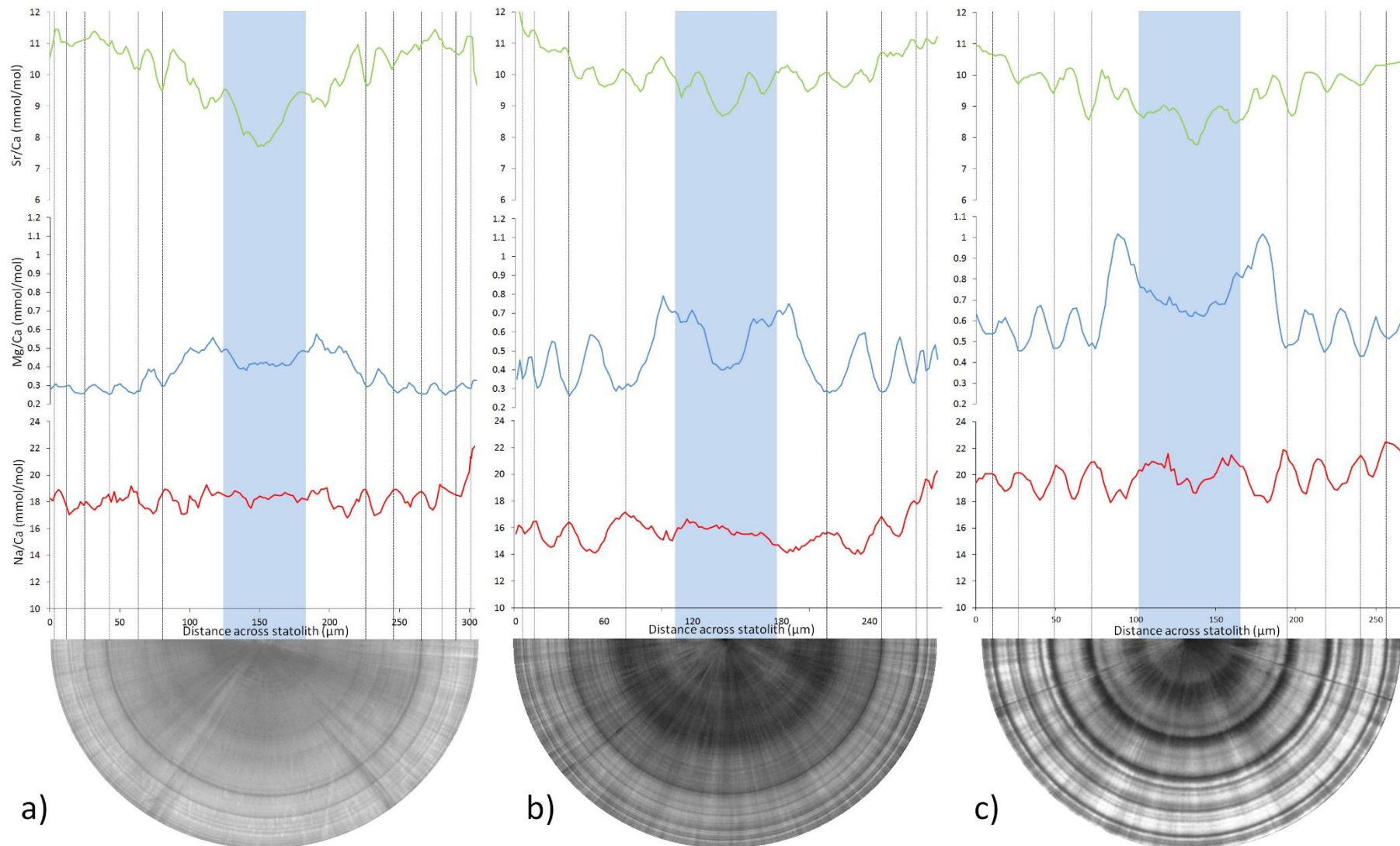


748

749 Figure 4. The intensity of a selection of XRD peaks across the diameter of two statoliths (a) statolith from a field-
 750 collected adult specimen and (MS13-13) and (b) a juvenile laboratory reared specimen (TB-1), overlaid on
 751 photomicrographs of the corresponding statoliths. The blue shaded areas represent the distance covered by the
 752 hatching ring. Y-axes are presented arbitrary units of intensity.



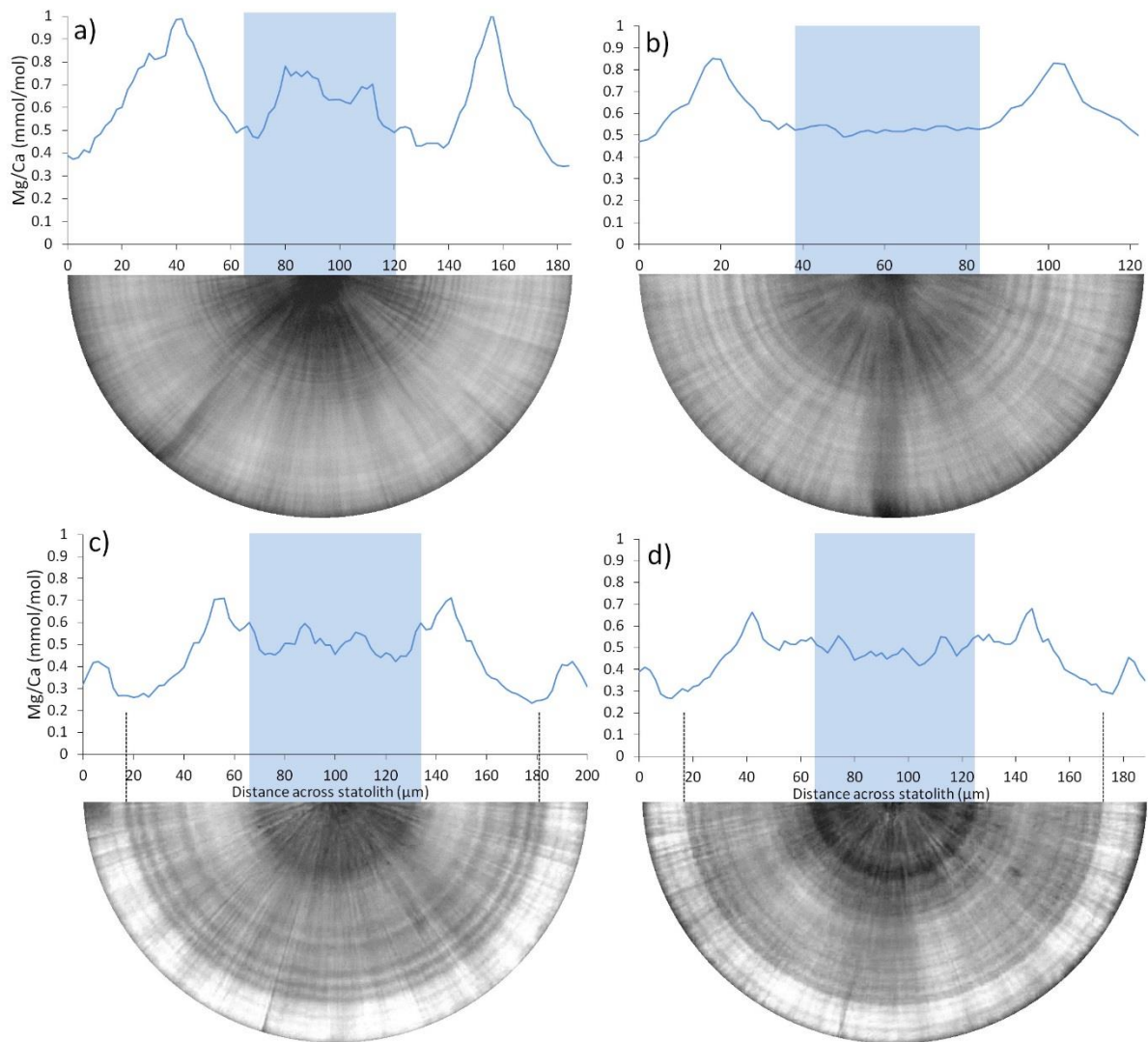
753
 754 Figure 5. SEM images of a fractured statolith segment. The dorso-ventral axis is highlighted with a dashed yellow line, (a) growth rings can clearly be seen within the exposed
 755 surfaces (black arrows) and (b) a magnified image of the nucleus area highlighted by the red box in (a) showing a clear 'hour glass' shape in the crystal structure within this
 756 region. The blue dashed lines highlight the hourglass shape of the microstructure.



757
758
759
760

Figure 6. Photomicrographs of ground and polished statoliths from field-collected male *Buccinum undatum* from Shetland (a), the Menai Strait (b) and Jersey (c). The overlaid plots display the strontium (green lines), magnesium (blue lines) and sodium (red lines) profiles across each statolith. Blue areas represent larval growth inside the hatching ring. Vertical black lines above the statolith indicate the positions of the growth rings. All data are presented as mmol/mol ratio to Ca^{44} .

761



762

763 Figure 7. Photomicrographs of ground and polished statoliths from laboratory reared *Buccinum undatum*,
764 overlaid with profiles of the Mg/Ca ratios determined using SIMS. (a & b) statoliths from one –year-old whelks
765 of two sizes (a = 31 mm shell length; b = 11 mm shell length) and (c & d) statoliths from two-year-old whelks of
766 two sizes (c = 52 mm shell length; d = 35 mm length). Blue areas represent larval growth inside the hatching ring.
767 All data are presented as mmol/mol ratio to Ca⁴⁴.

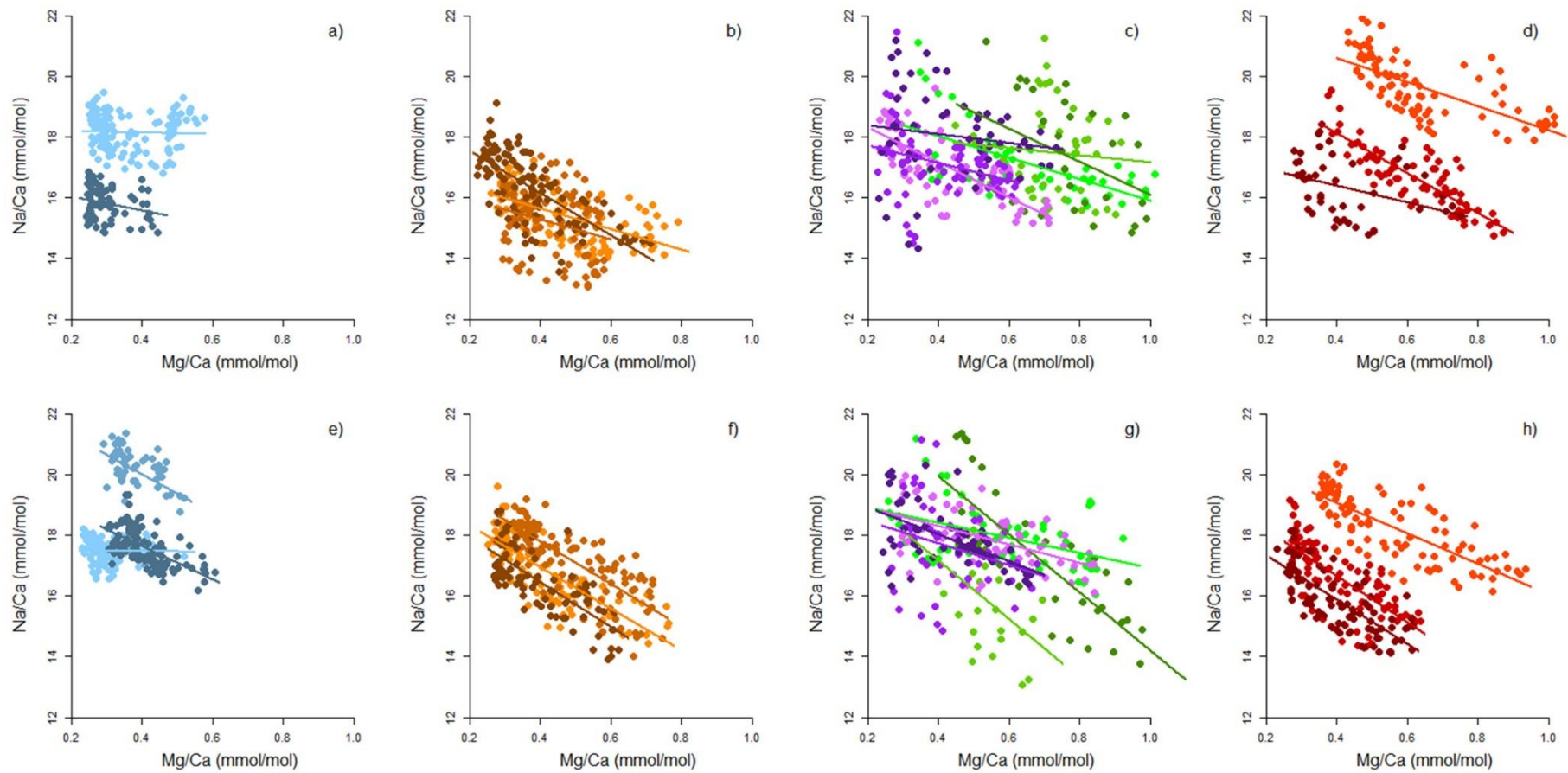
768

769

770 Table 1. Summary data from the combined elemental profiles in statoliths from each site. Data are presented as a mmol:mol ratio to Ca⁴⁴

	Tank one-year-olds			Tank two-year-olds			Shetland Isles			Menai Strait			Jersey		
	Na/Ca	Mg/Ca	Sr/Ca	Na/Ca	Mg/Ca	Sr/Ca	Na/Ca	Mg/Ca	Sr/Ca	Na/Ca	Mg/Ca	Sr/Ca	Na/Ca	Mg/Ca	Sr/Ca
Mean	17.64	0.65	9.11	17.57	0.45	9.45	17.70	0.35	10.28	16.18	0.46	9.79	17.26	0.50	10.18
Max	24.51	1.12	10.87	21.50	0.84	11.36	21.39	0.61	12.49	19.62	1.10	12.36	21.93	1.02	11.91
Min	13.08	0.26	7.70	14.36	0.23	8.05	14.86	0.23	8.92	13.10	0.22	7.83	14.13	0.23	8.24
Range	11.43	0.86	3.18	7.14	0.61	3.30	6.52	0.38	3.57	6.52	0.88	4.52	7.80	0.79	3.66

771



772
 773 Figure 8. Scatter plots showing relationships between Mg/Ca and Na/Ca ratios in statoliths from individual whelks. The samples from Shetland are shown with blue markers
 774 for males (a) and females (f), samples from the Menai Strait are shown with brown markers for males (b) and females, samples from laboratory growth experiments are
 775 shown as purple (one-year-olds) and green (two-year olds) for males (c) and females (g) and samples from Jersey are shown with red markers for males (d) and females (h).
 776 Coloured lines represent linear relationships between datasets of the same colour.

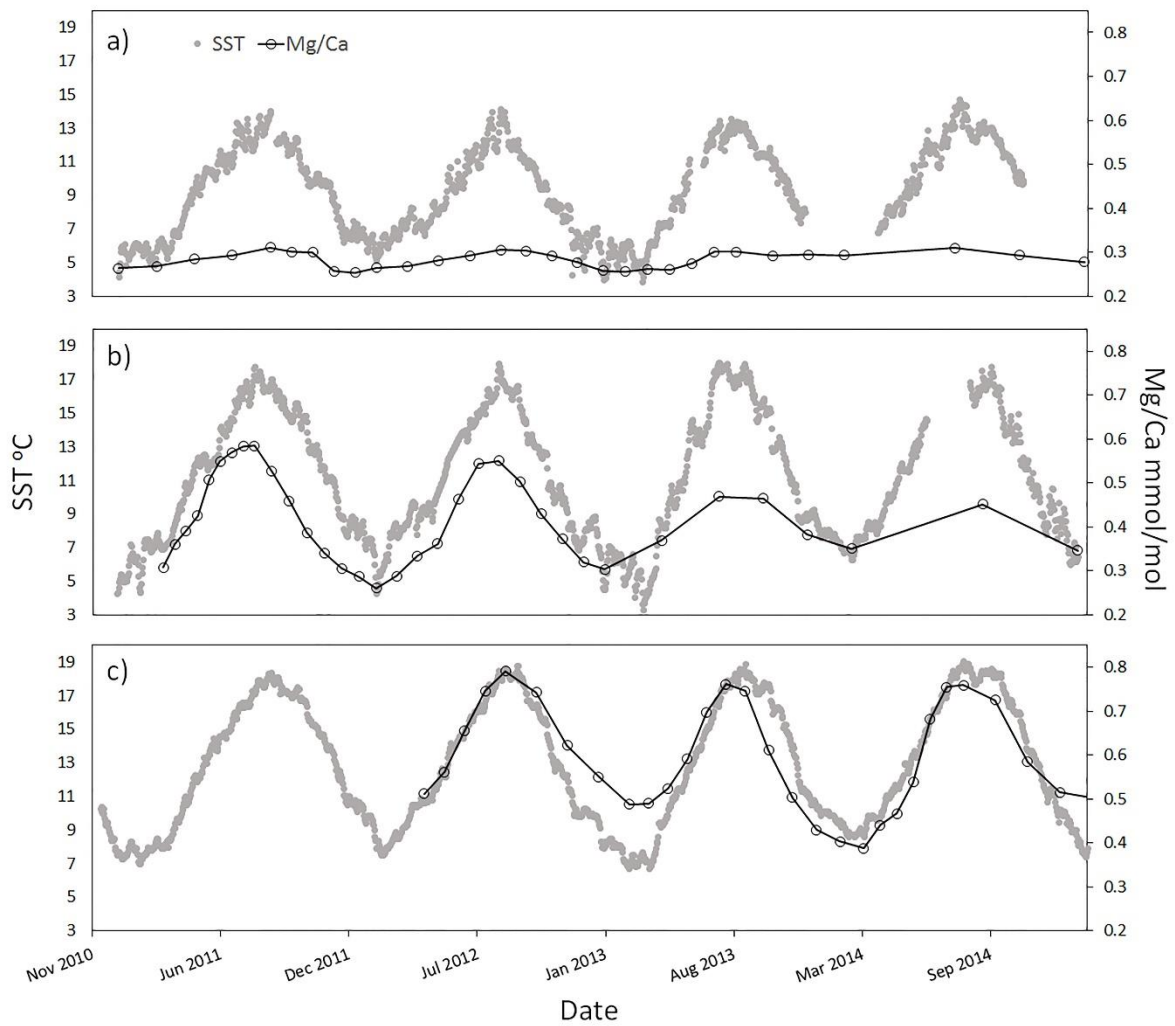


Figure 9. Sea surface temperature profiles (grey dots) overlaid with Mg/Ca ratio data (black line, unfilled circles) from SIMS analysis of a single representative statolith from each site (a) Shetland; b) Menai Strait; c) Jersey). The higher innermost cycles of the Mg/Ca profiles have been removed for easier visual comparison. The primary and secondary axes of all three plots are set to the same ranges for comparison.

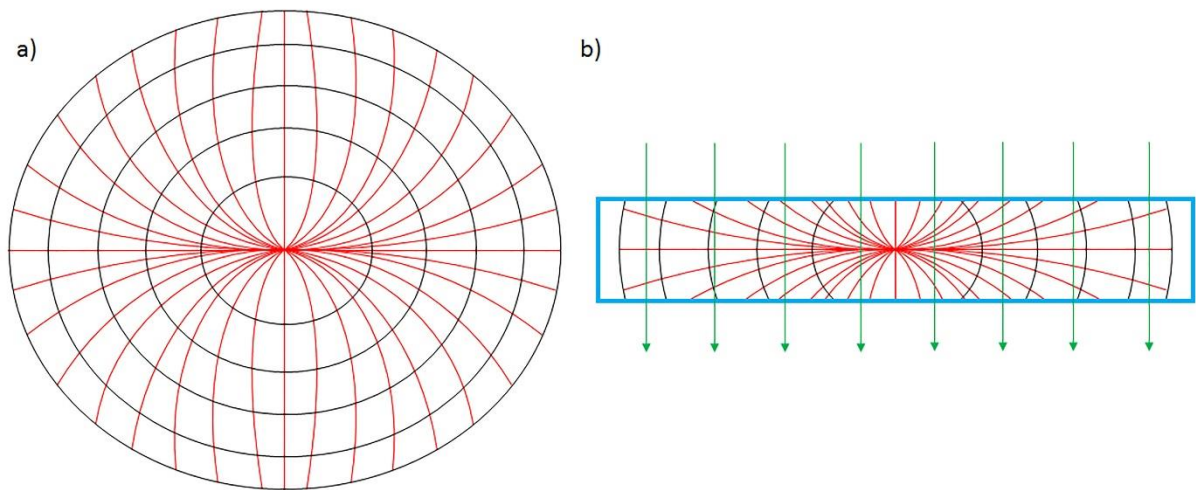
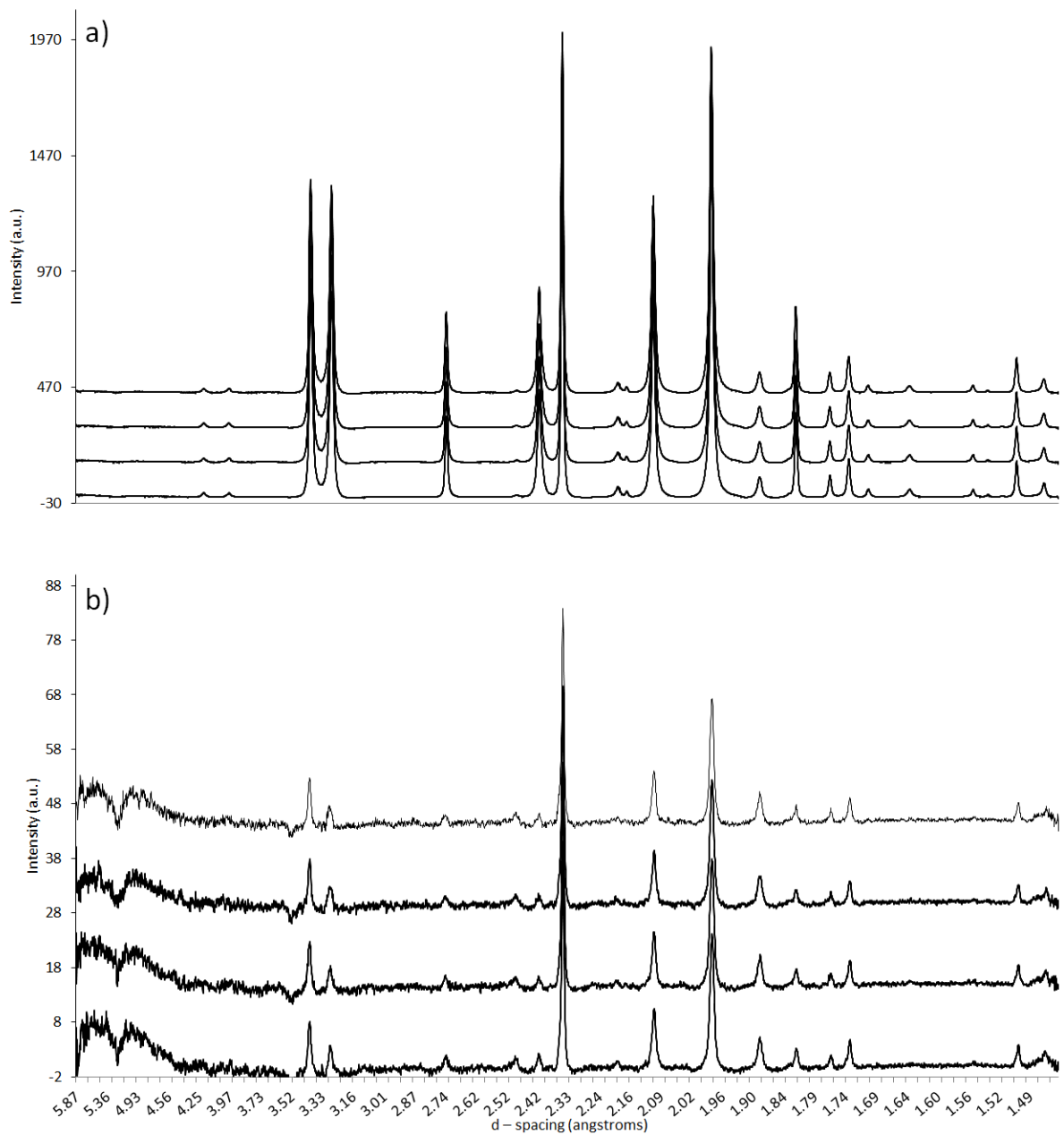
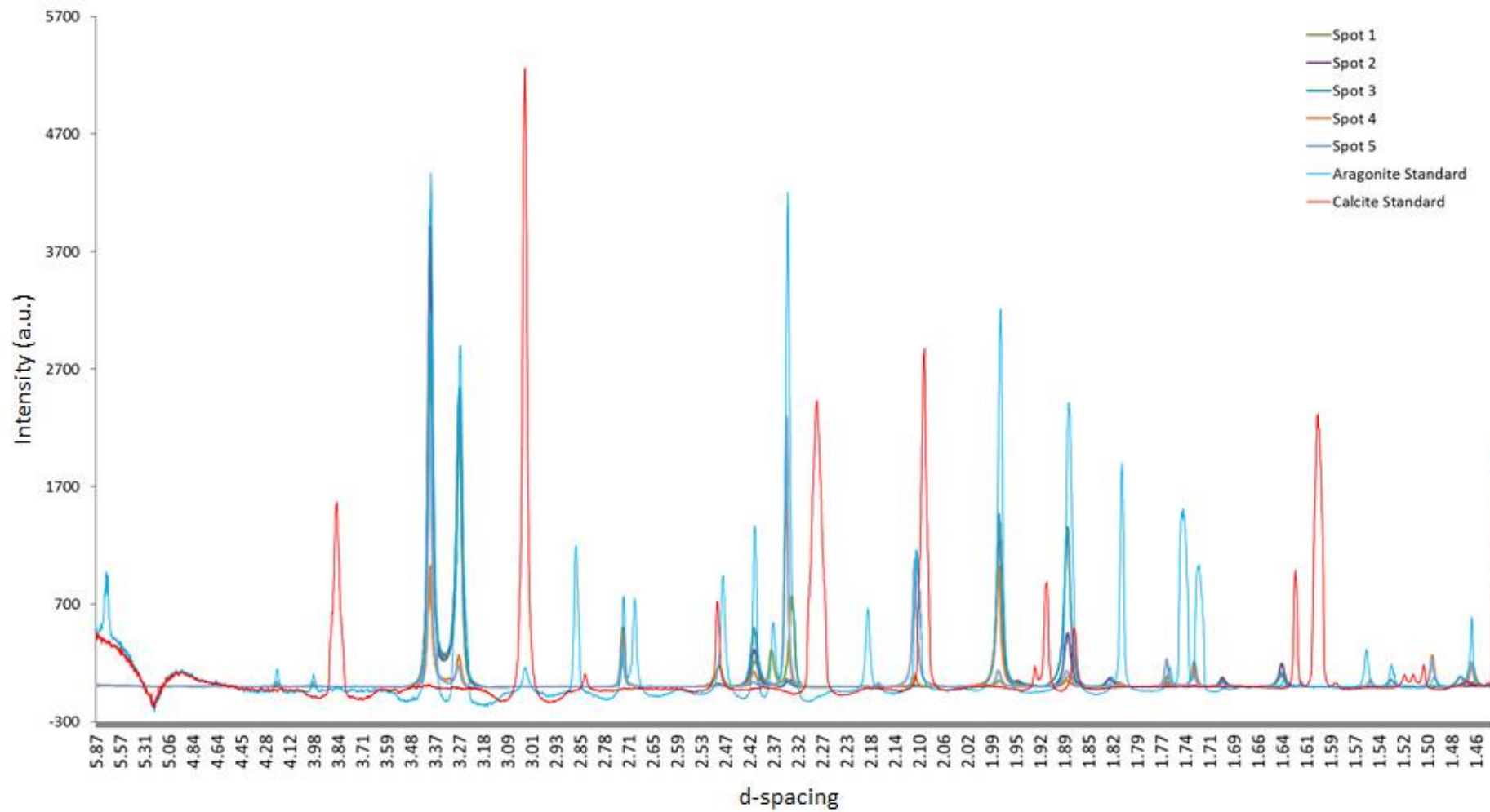


Figure 10. a) A diagrammatic representation of the 'hourglass' crystal structure of a *Buccinum undatum* statolith. The black circles represent the statolith growth rings and the red lines represent crystal orientations and b) a diagrammatic representation of a thin section (blue box) of the *Buccinum undatum* statolith shown in (a) indicating the crystals sampled during μ XRD. The green lines represent the passage of X-rays.

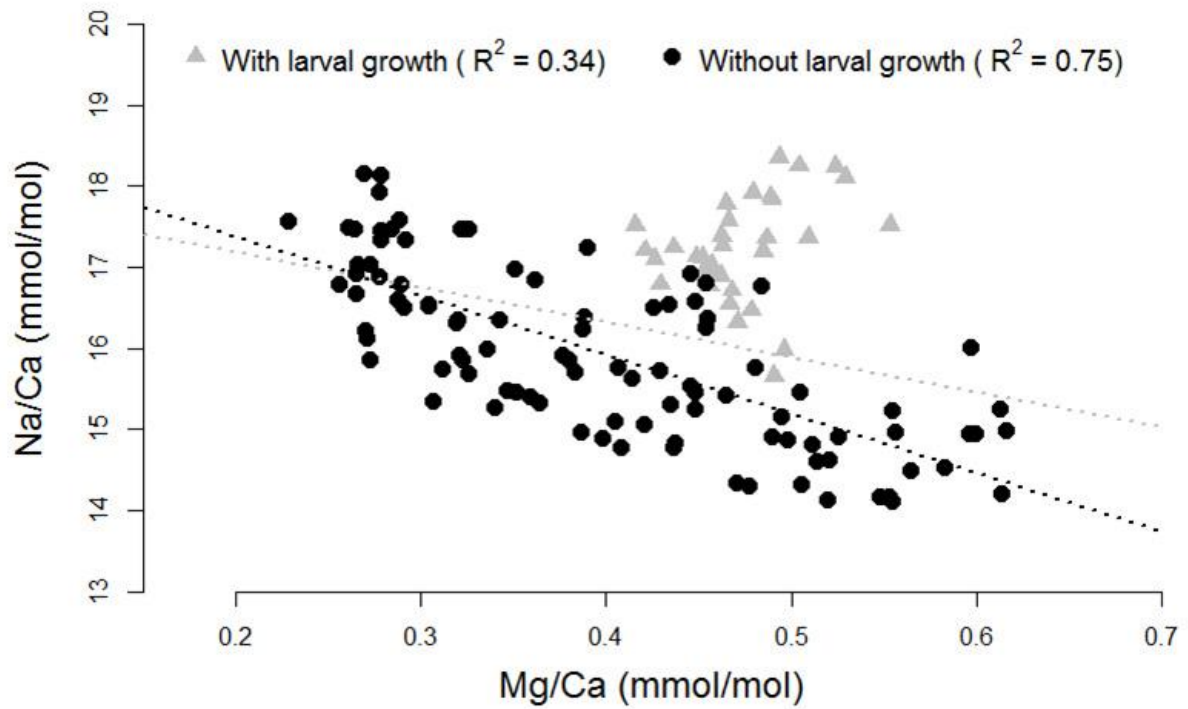
Supplementary material



SMFigure 1. Stack plots of 4 successive XRD profiles taken at 30 second intervals at the same location, a total of 12 profiles were taken one every 10 seconds but only 4 are presented. a) shows data from the centre of a statolith from the Menai Strait and b) shows data from close to the edge of the same statolith. Note the differences in intensity between the edge and centre data.



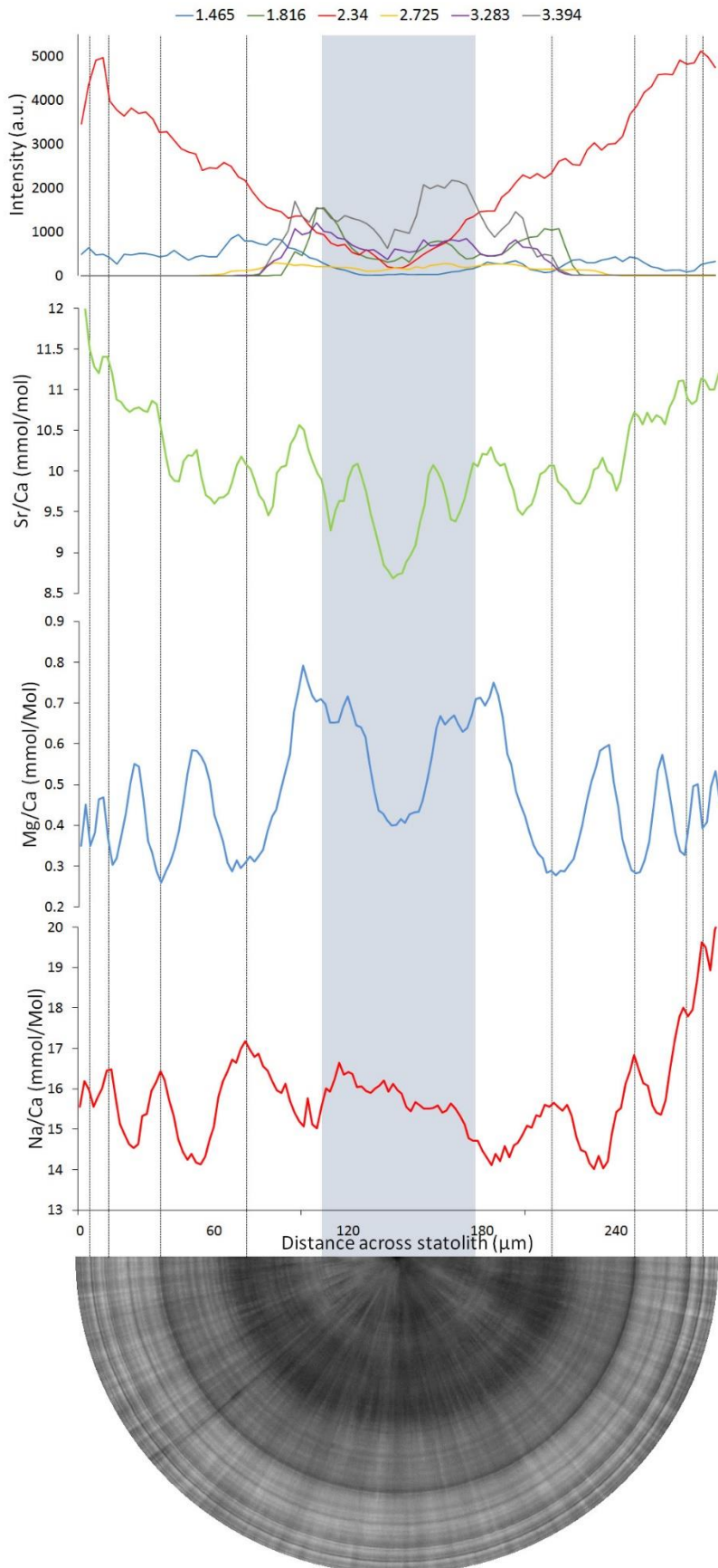
SMFigure 2. Stack plot of XRD profiles taken at $\approx 20 \mu\text{m}$ spacing along the growth axis of a single broken (unprocessed) *B. undatum* statolith. The stacked sample profiles are overlaid with profiles from aragonite (light blue) and calcite standards (red).



SMFigure 3. A scatter plot of Na/Ca against Mg/Ca for a single statolith (JF4-8). Black circular dots represent data from post hatching growth. Grey triangular dots represent data from within the hatching ring (larval growth). The black dotted line shows the linear relationship between the two elements without the larval growth data. The grey dotted line is the linear relationship between the two elements including the larval growth.

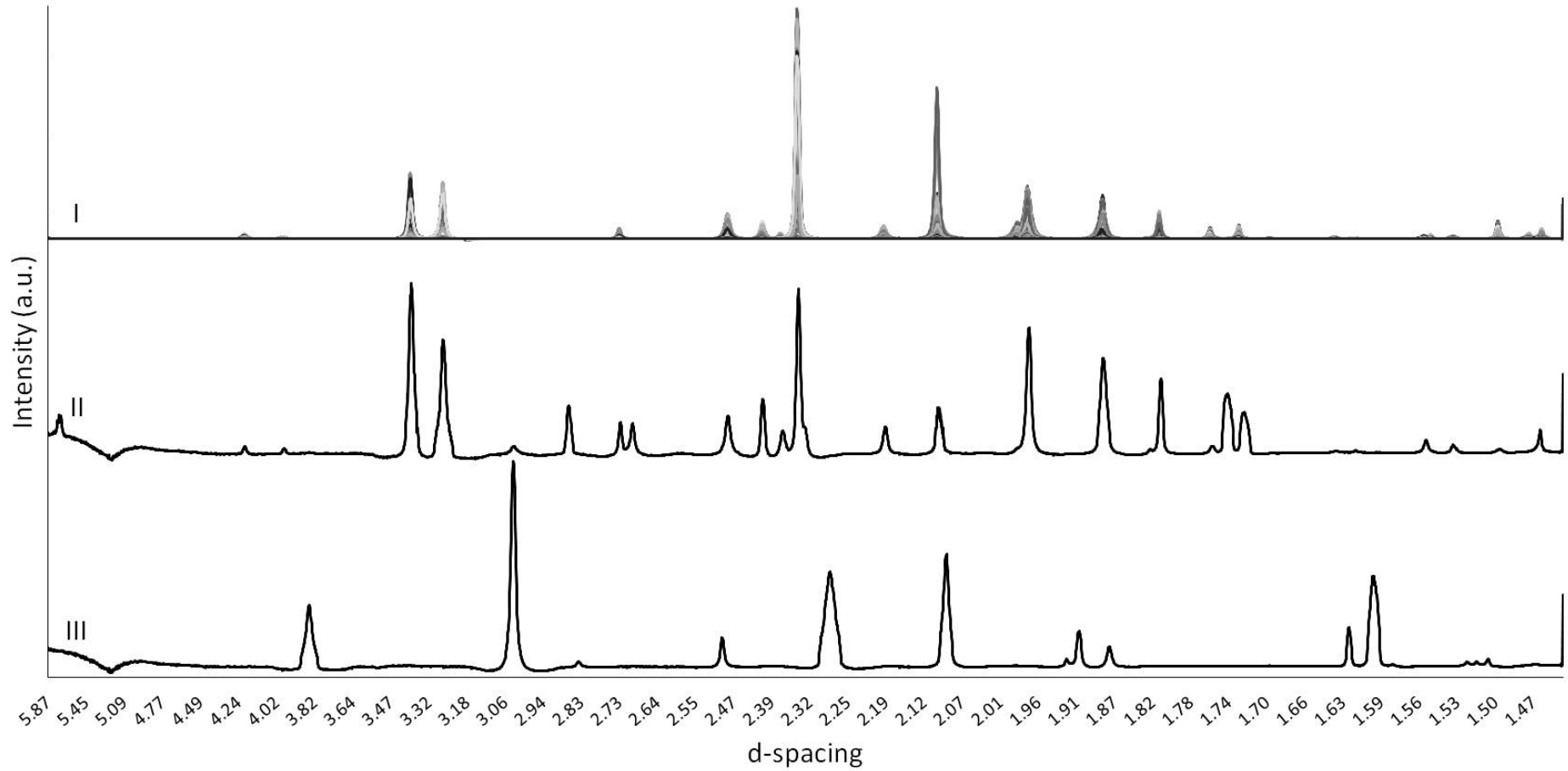
SMTable 1. Pearson's correlation coefficients of the relationships between elemental-to-calcium ratio profiles in statoliths from male and female *Buccinum undatum* reared in the laboratory and from the Menai Strait, Jersey and Shetland. Correlation strength is shown by colour, grey = 'weak', yellow = 'moderate' and orange = 'strong'. Significance, ** = $p < 0.001$, * = $p < 0.05$.

	Laboratory year 1 Male			Laboratory year 1 Female			Laboratory year 2 Male			Laboratory year 2 Female		
	TB1	TB2	TS1	TB3	TS2	TS3	TB1-2	TB3-2	TS1-2	TB2-2	TS2 - 2	TS3-2
Na/Ca vs. Mg/Ca	-0.61**	-0.51**	-0.4*	-0.45**	-0.44*	-0.79**	-0.7**	-0.32*	-0.14	-0.52**	-0.29*	-0.55**
Na/Ca vs. Sr/Ca	-0.2	0.2	-0.14	0.33*	-0.66**	-0.83**	0.06	0	-0.39*	-0.07	-0.14	0.35*
Sr/Ca vs. Mg/Ca	0.06	-0.09	-0.34	-0.48**	0.58*	0.74**	0.01	-0.48**	-0.51**	-0.22	-0.43**	-0.49**
	Menai Strait Male			Menai Strait Female			Jersey Male			Jersey Female		
	MS13-3	MS13-13	MS13-33	MS13-7	MS13-22	MS13-23	JF4-4	JF4-5	JF4-9	JF4-6	JF4-7	JF4-8
Na/Ca vs. Mg/Ca	-0.59**	-0.27*	-0.69**	-0.81**	-0.77**	-0.74**	-0.67**	-0.84**	-0.36**	-0.77**	-0.71**	-0.75**
Na/Ca vs. Sr/Ca	0.22*	0.25*	0.13	-0.34*	-0.4**	0.225	-0.2*	-0.23*	-0.57**	-0.06	-0.13	-0.07
Sr/Ca vs. Mg/Ca	-0.05	-0.16	-0.12	0.32*	0.01	0.03	-0.15	-0.02	-0.18	0.36**	-0.31*	-0.2*
	Shetland Male			Shetland Female								
	SH-19	SH-25	SH-26	SH-30	SH-31	SH-32						
Na/Ca vs. Mg/Ca	-0.04	-0.01	-0.43**	-0.62**	0.67**	-0.24*						
Na/Ca vs. Sr/Ca	-0.28*	-0.17	-0.37**	-0.19	0.81**	-0.06						
Sr/Ca vs. Mg/Ca	-0.78**	-0.19*	-0.1	-0.04	0.5**	-0.13						



SMFigure 4. A combined plot of the diffraction data presented in Figure 4 (top plot) and the elemental data presented in Figure 6 (bottom three plots), overlaid on a photomicrograph of the analysed statolith. Black lines denote the annual growth rings.

1



2

3 SMFigure 5. Stacked XRD spectra from I) 110 successive combined analyses across the centre of a single statolith, II) the speleothem aragonite standard, III)

4 the synthetic calcite standard. The combined statolith data shown in I) bears a clear resemblance to the aragonite standard shown in II).

5

6